Chapter: 4

Results and discussion

Results and discussion on the work carried out in the present study has been divided into three sections as given below:

Section I: Comparative study of hydrogen production from steam reforming of acetic acid over synthesized catalysts via MOF and wet impregnation methods

Section II: Effect of Ni loading on catalytic activity and products distribution for acetic acid steam reforming over nickel-based catalyst synthesized via MOF process

Section III: Activation, Deactivation and Kinetic studies

The section wise results and discussion are presented in following pages

I

Section: I

Comparative study of hydrogen production from steam reforming of acetic acid over synthesized catalysts via MOF and wet impregnation methods

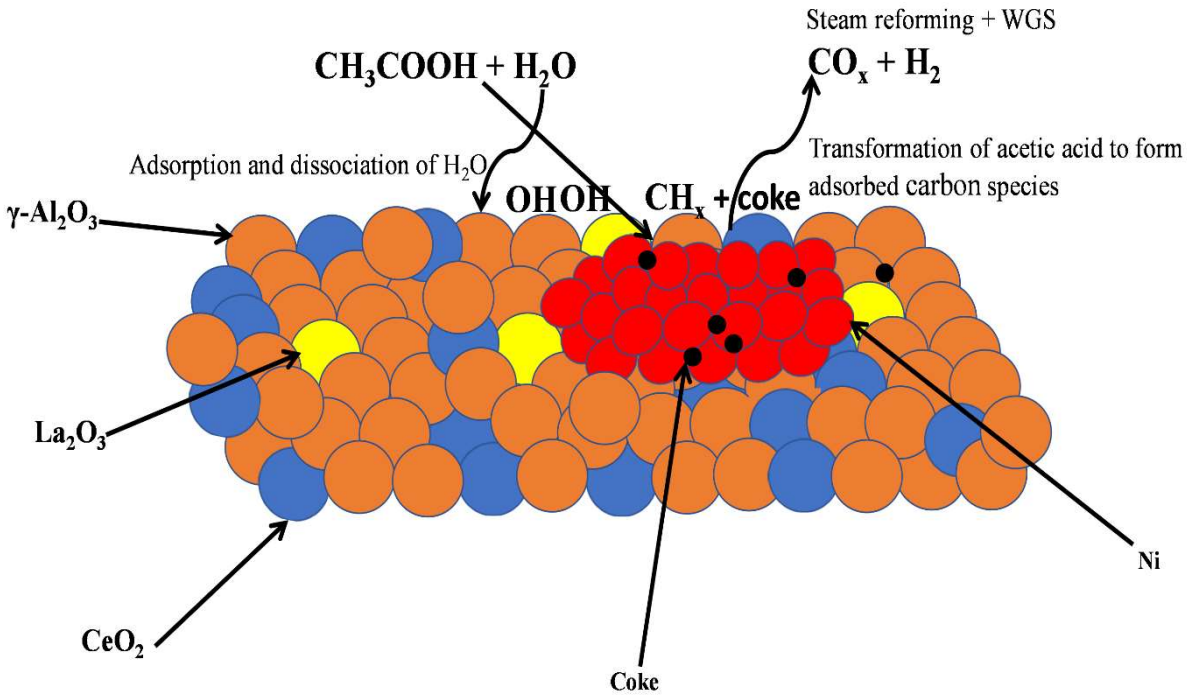

In the present study, Ni/γ-Al_2O_3 catalysts impregnated with La_2O_3-CeO_2 have been prepared from two different methods (i) via MOF (Catalyst 1) and (ii) wet impregnation method (Catalyst 2) as listed in Table 3.1. Their catalytic activity and stability were evaluated in AASR for hydrogen production at different temperatures ranging from 300 to 650 ºC, with fixed S/C ratio = 6.5 and weight hour space velocity (WHSV) 1.05 h^{-1} and time on stream (TOS). The stability test for acetic acid conversion and product distribution were observed for 36 h of TOS for both catalysts. The results showed that the catalyst prepared using the MOF precursor showed a better yield of H_2 and stability against coke deposition due to regular pore structures and more no of oxygen molecules available on MOF derived catalyst's surface. The yield of H_2 was found to be approx. 90%, i.e., close to the theoretical stoichiometric limit. Very low CH_4 selectivity was observed in both catalysts at high temperatures. Various characterizations were applied to ascertain the chemical and textural properties of both the prepared catalysts, including X-ray diffraction (XRD), H_2 temperature program reduction (TPR), transmission electron microscopy (TEM), Scanning electron microscope (SEM-EDAX), BET surface area by N_2 adsorption-desorption, and thermogravimetry analysis (TGA). Results are discussed below.

4.1. Characterization of precursors

Fig 4.1 presents the TG-DTA analysis of $Ni(HCOO)_2.2H_2O$ performed from 23–1000 °C at a rate of 10 °C/min in an inert (N_2) atmosphere. It shows that the decomposition was a two-step process. In the first step, water molecules were removed at 200 ºC and next, the anhydrous formate decomposed to Ni at 285 ºC. The final weight was 32.6% of the initial sample, which matched nickel content (32.9%) in $Ni(HCOO)_2.2H_2O$. Thus, it confirms that the nickel formate decomposed directly to metallic nickel in an inert atmosphere.

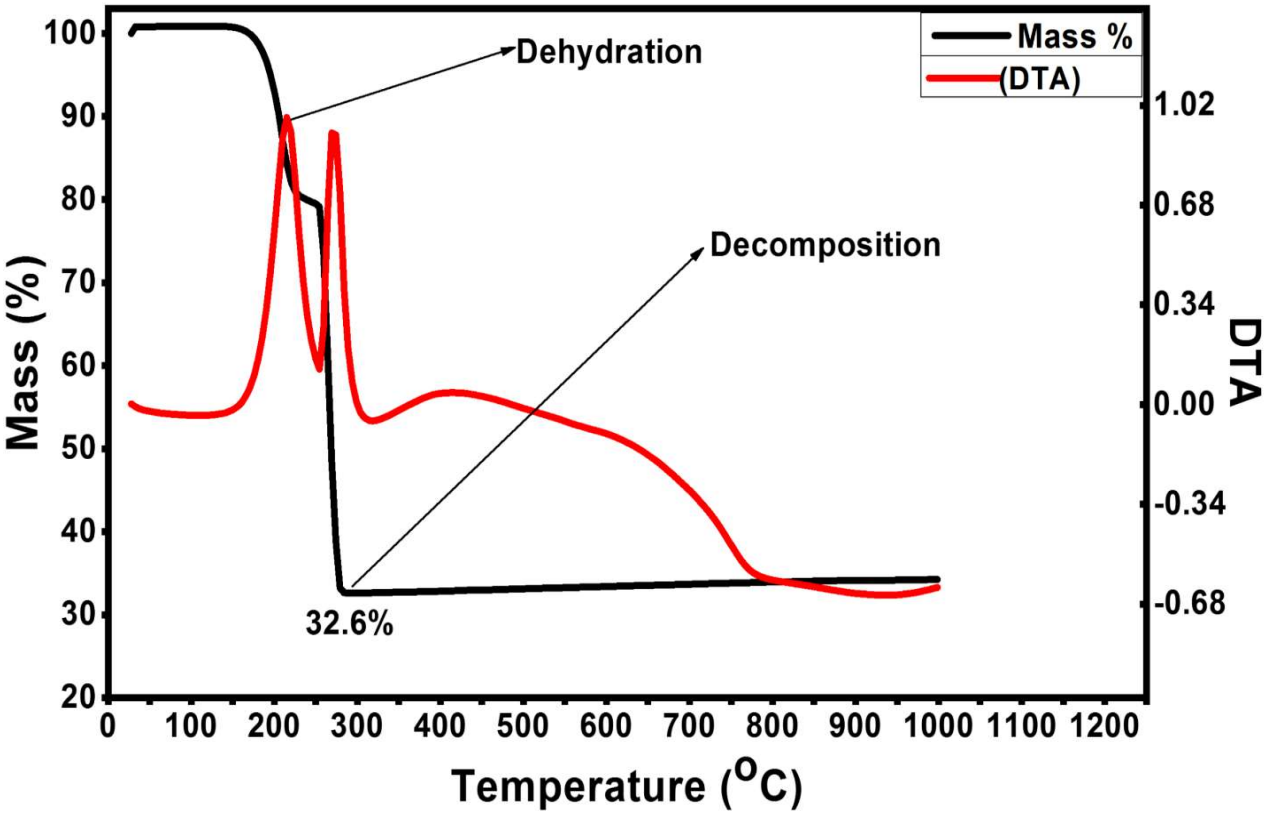

Fig. 4.1. TGA profiles of nickel formate ($Ni(HCOO)_2).2H_2O$)

DT-TGA analyses of prepared $[Ni(2'2'\text{-bipy})_2Cl_2].6H_2O$ (**Fig. 4.2)** showed that the

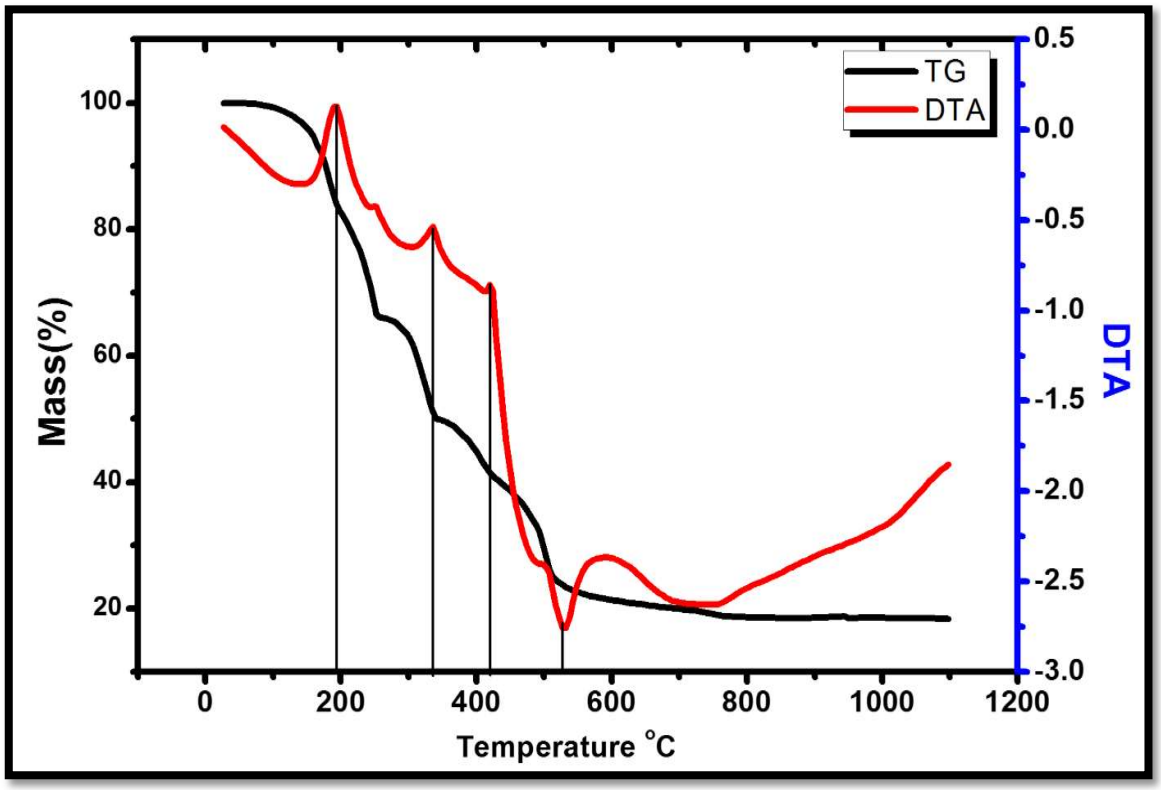

Fig. 4.2. TGA and DTA profiles of Ni-complex

precursor of nickel complex finally decomposed to Ni with the removal of different volatile compounds. The first decomposition peak at ~200 °C is attributed to the removal of H_2O coordinated with complex molecules along with 29.38% mass loss. The remaining three successive decomposition peaks attributed to the removal of bipyridine, hydrogen chloride and chlorine molecules with a residue of 18.32% that is assigned to nickel-metal Ni. A similar report has been reported by Mazhar et al.[276].

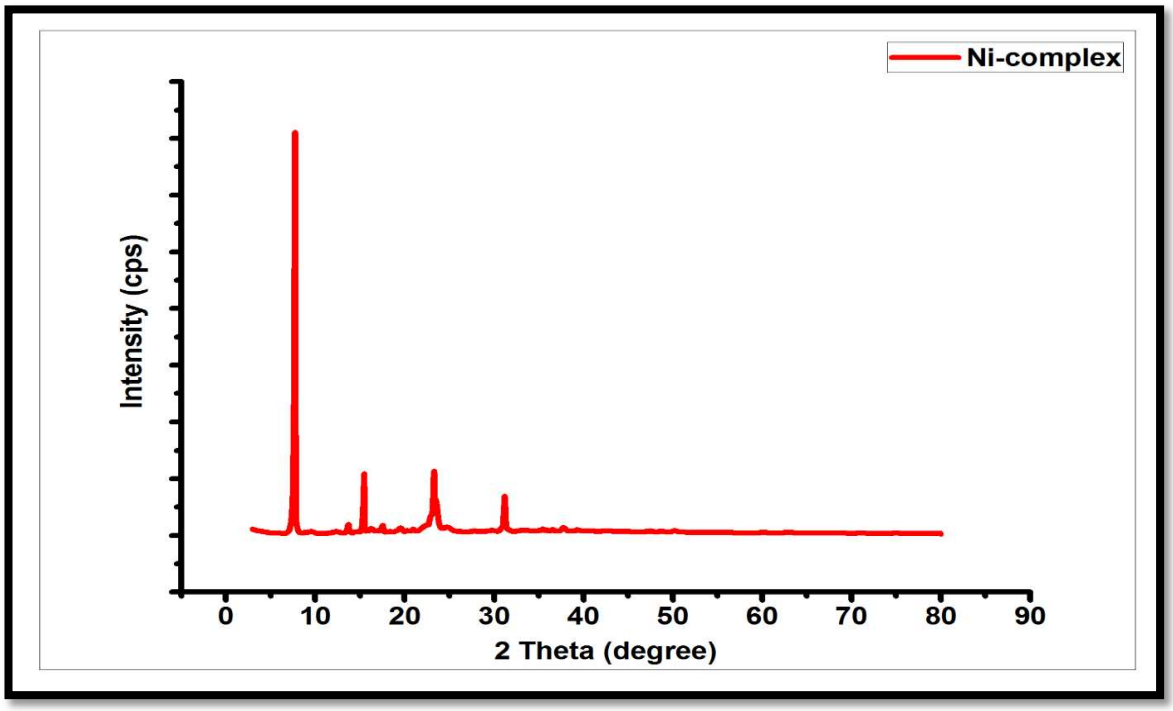

Fig. 4.3: XRD pattern of the monometallic complex of Ni

Fig. 4.3 illustrates the powder diffraction pattern (XRD) of nickel $[Ni(bipy)_2]Cl_2$ complex prepared through MOFs method. No clear evidence of free 2,2′ bipyridine (Ref. Code 00-015-1119), metal atoms (Ni) and/or; salts was observed. It was believed that the metal salts reacted completely with the ligand to form the complex, and the amounts of unreacted quantities were too little to be detected by XRD [277]. A similar result was also observed that in the related ligand 2'2' bipyridine forms a bis- (chelated) complex with metallic Ni,

$$Ni[(bpy)_2]Cl_2 \longrightarrow Ni[(bpy)]\ Cl_2 \longrightarrow NiCl_2 \longrightarrow NiCl \longrightarrow Ni \quad (1)$$

connected with hydrogen bonding The crystal structure of the compound shows monoclinic unit cell [278]. It is also observed that the complex of nickel and ligand 2'2' bipyridine prepared by MOF process gives metallic Ni only after its decomposition in inert atmosphere. The proposed thermal decomposition process of Ni-complex nanoparticles is given in Eq. 1 [276].

4.2. XRD analysis of Catalysts

XRD patterns of Al_2O_3, ALC (Al_2O_3-La_2O_3-CeO_2), catalyst-1, and catalyst-2 are presented in **Fig. 4.4.** Several peaks related to supports and nickel were identified with their d-value (calculated using Bragg's law) and matched with the standard values. It is observed that peaks corresponding to γ-Al_2O_3, CeO_2, and Ni, metal is only present. The modified supports and prepared catalysts showed diffraction peaks at around 2θ = 37.2°, 45.8°, and 66.7°, which were assigned to γ-Al_2O_3 (JCPDS 86-1410). The three high-intensity peaks of Ni observed at 44.5°; at 51.8° and 76.5° correspond to (111), (200) and (220) planes. The absence of the characteristic nickel (II) oxide (NiO) peaks (2θ = 37.3° and 43.3°) from any of the catalyst samples indicates that both Ni precursors exclusively provide metallic Ni sites after calcining in the inert atmosphere on the catalyst surface. The characteristics peaks of cubic fluorite crystal structure of CeO_2 was dominant and observed at 2θ =28.30° (111), 33.13° (200), and 56.33° (311) in catalyst-1, catalyst-2, and support ALC, respectively, which typically indicating the segregation of the CeO_2 over the γ-Al_2O_3 [279]. Cubic fluorite structures also help to diffuse more oxygen and formation of oxygen vacancy[99]. Peaks of La_2O_3 corresponding to crystalline species of La_2O_3 were not observed in either catalysts or the support ALC, probably due to its well dispersion and low amount in the samples or low crystallite size[45]. The Crystallite size of Ni catalysts was calculated by Scherrer equation for the (200) peak, as shown in **Table 4.1.** It is observed from Table 4.1 that the crystallite size of Ni in catalyst 2 (prepared via MOF) had average

crystallite of 37 nm, which is nearly 2.5 times that of catalyst 1 (prepared from nickel formate).

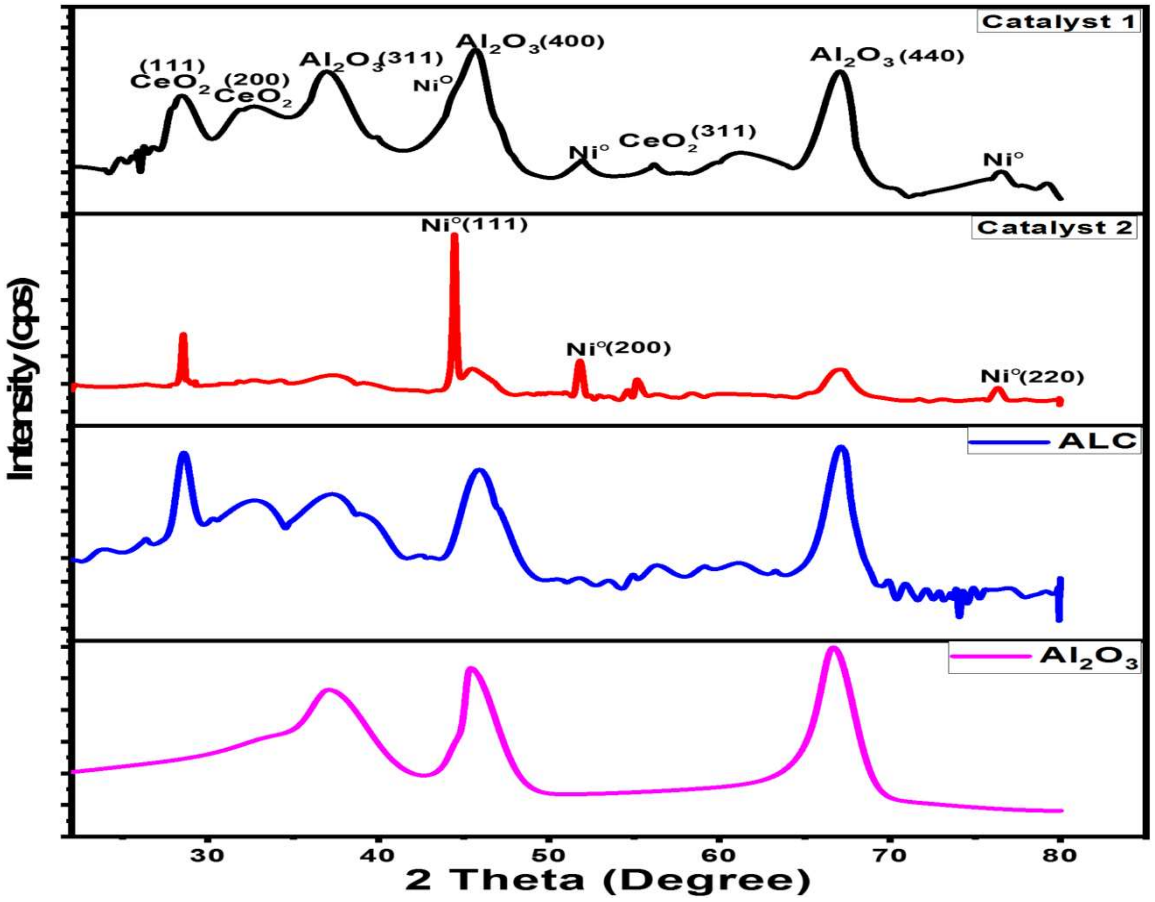

Fig. 4.4: XRD Patterns of Alumina, ALC, Catalyst 1 and Catalyst 2

4.3. TPR Analysis

Fig. 4.5 illustrates the H_2-TPR patterns and reduction degree of both catalysts. The results show that typically nickel species in both catalysts were fully reduced in the temperatures range 400 to 600 ºC. Fig. 4.5 also shows the reduction temperature of pure nickel oxide sample, prepared from calcination of ($Ni(HCO_2)_2.2H_2O$) in the presence of air at 650 ºC, was found at 329 ºC, which referred to as "free" nickel oxide[281]. TPR explains the reduction behavior of Ni depending on interactions with support. The reduction temperature (the maximum peak) for NiO in the catalyst-1 increased to 461 ºC while reduction of catalyst 2 was observed in two stages; two earlier peaks appeared for catalyst-2 occurring at 406 and 437 °C, which also assigned to the reduction of NiO phase to Ni.

The low-temperature peak is attributed to the reduction of the relatively free NiO particles, and the high-temperature peak is attributed to the reduction of NiO with support interaction. The results are showing weak to medium interaction with the prepared support. Similar Ni with Al_2O_3 support interactions was also reported by various researchers [45, 282, 283]. No reduction peaks corresponding to the spinel ($NiAl_2O_4$) phase appeared because both catalysts were calcined at 650 ºC temperatures, and [284] it was also well reported that Ni and alumina particles could only react to form spinal phase at above 800 °C[285, 286].

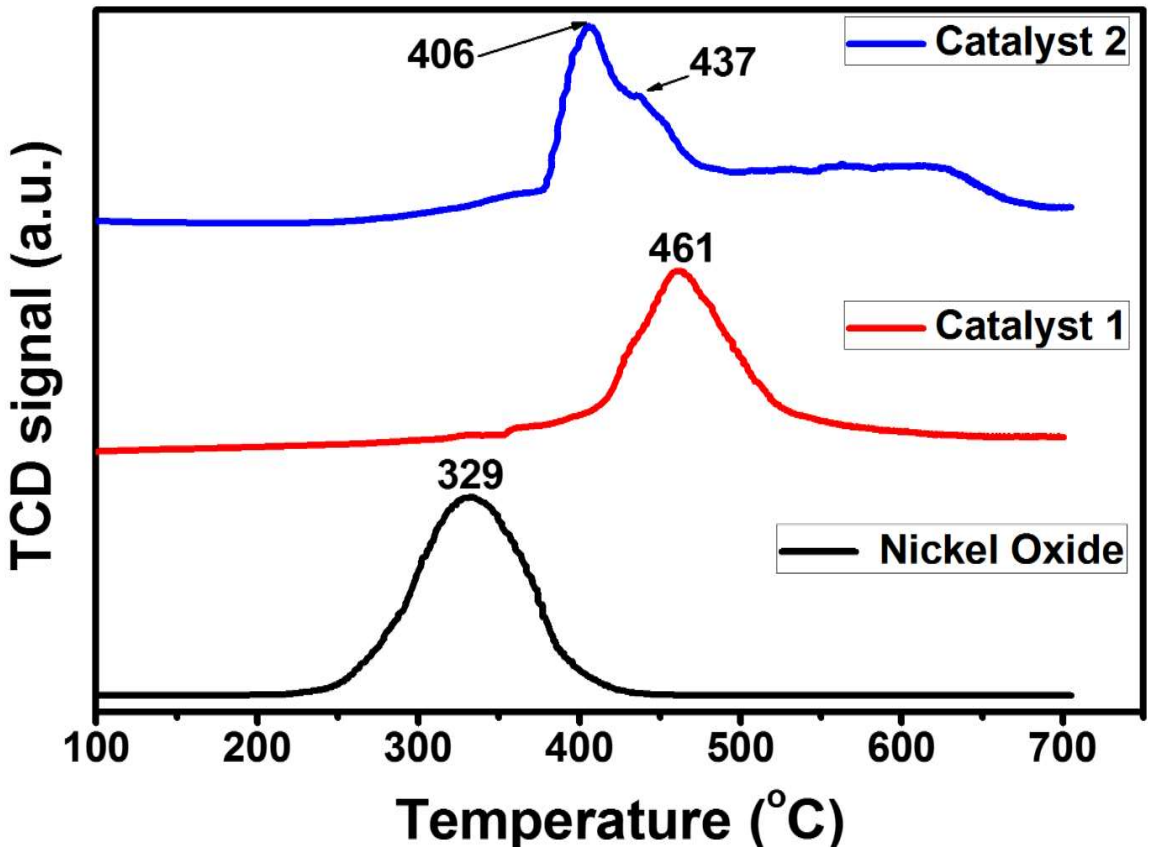

Fig. 4.5. TPR profiles of Catalyst 1, Catalyst 2, and nickel oxide

Moreover, bond formation between Ni atom and La atom also prevented the formation of spinel $NiAl_2O_4$ structure and maintained the Ni as active sites over the surface[247]. Some authors also reported that the incorporation of CeO_2 and La_2O_3 promoters weakened the NiO-Al_2O_3 interaction and facilitated the Ni species reduction earlier [45, 287, 288]. Consequently, the strong interaction of Ni species with the γ-Al_2O_3 was significantly

inhibited in both catalysts. Catalyst-1 showed only one reduction peak near 461ºC, showing a medium interaction with support. However, in the case of catalyst-2, two earlier reduction peaks at 406 and 437, respectively, showed a large number of "free" nickel oxide particles available on the support surface and weak interaction with the support, resulting in high activity than Catalyst-1.

4.4. Surface area and pore size analysis

Table 4.1 represents the synthesized support and catalysts' textural properties, as it can be observed that incorporation with La_2O_3 and CeO_2 resulted in a lower surface area, pore volume, and average pore size. It is noticed that γ-Al_2O_3 has a high surface area of 169 m^2/g, whereas, on the incorporation of La_2O_3 and CeO_2, its surface area reduced to 133 m^2/g. In addition, further loading of 15wt% Ni also decreased surface area to 110 and 120 m^2/g for catalyst-1 and catalyst-2, respectively. It is further observed that the γ-Al_2O_3 has a total pore volume of 0.61 cm^3/g whereas, it is significantly lower at 0.43 cm^3/g for synthesized ALC support. It is also observed that the total pore volume of both catalysts and is also significant decreased viz 0.27 and 0.29 cm^3/g on incorporating Ni for catalyst-1 and catalyst-2, respectively.

Table 4.1. Textural properties of synthesized catalysts:

Support/Catalyst	Surface area (m^2/g)	Pore volume (cm^3/g)	Average pore size (nm)	Crystallite size of Ni[a] (nm)
γ-Al_2O_3	169	0.61	9	-
Al_2O_3-La_2O_3-CeO_2 (ALC)	133	0.43	8	-
15%Ni/ALC	110	0.27	9	14
15%Ni-comp/ALC	120	0.29	8	37

[a] 200 plane

The pore size distribution of alumina (Table 4.2.) reveals its microporosity, with having the majority of pores of sizes less than 20 nm. While the incorporation of lanthanum oxide and cerium oxide, the microporosity reduced from 0.61 to 0.43 cm^3/g. Subsequently, when Ni was loaded on the support, the microporosity is further reduced. Since the surface area is also reduced with incorporating the above components, it is concluded that such components have also resulted in blockage of pores. Therefore, it is obvious that catalyst 2 has a large surface area and smaller pore size distribution suggesting that catalyst 2 possesses more active sites than catalyst 1.

Table 4.2. Pore size distribution of catalyst:

Species	**Pore size range (Å) and corresponding pore volume (cm^3/g)**					**Total pore volume (cm^3/g)**
	0≤dp≤10	10≤dp≤20	20≤dp≤40	40≤dp≤60	60≤dp≤80	
γ-Al_2O_3	0.29	0.22	0.05	0.03	0.02	0.61
15% Ni/ALC	0.06	0.07	0.06	0.02	0.06	0.27
15% Ni-Comp/ALC	0.09	0.16	0.02	0.008	0.01	0.29

dp (pore diameter)

4.5. TEM analysis of Catalysts

TEM analysis was performed to obtained structural detail of the prepared catalysts.

Results of transmission electron microscopy and corresponding electron diffraction patterns of catalyst 1 and catalyst 2 are shown in **Fig. 4.6 and Fig. 4.7**. The images of TEM clearly show that agglomerated small spherical type morphology corresponding to CeO_2. Moreover, dark road-type fringes were observed indicating alumina molecules, whereas

small black areas could be marked as metal Ni particles. It is also observed from the TEM micrographs that Ni particles in catalyst 2 are better dispersed compared to catalyst 1.

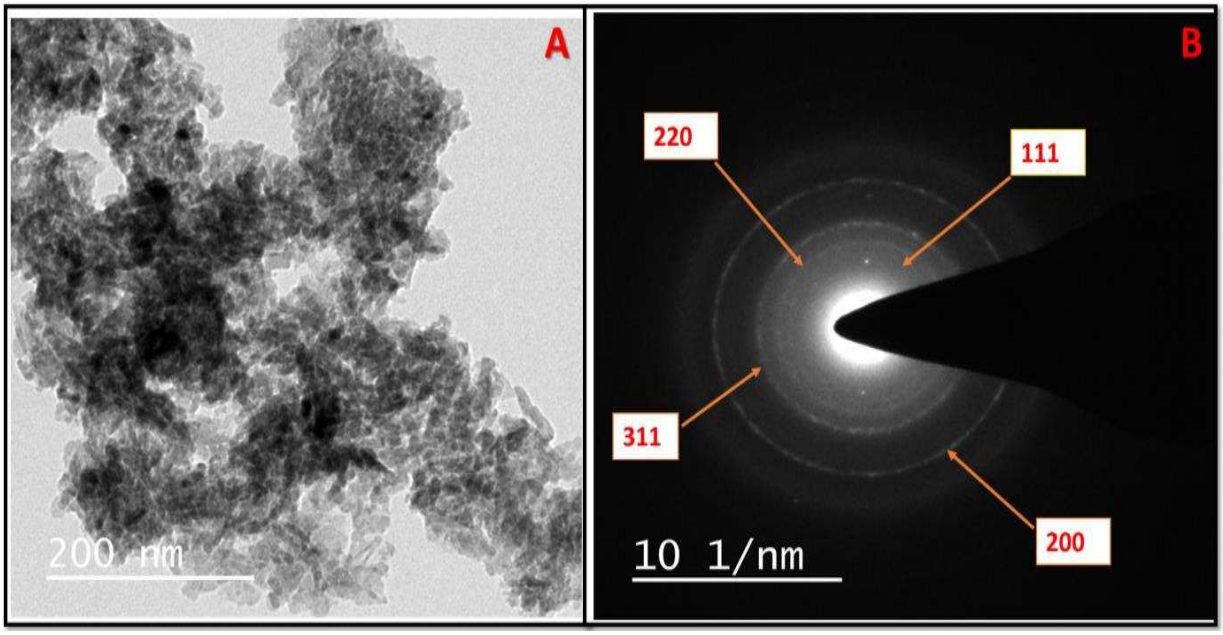

Fig. 4.6. TEM image and SAED diffraction of catalyst 1

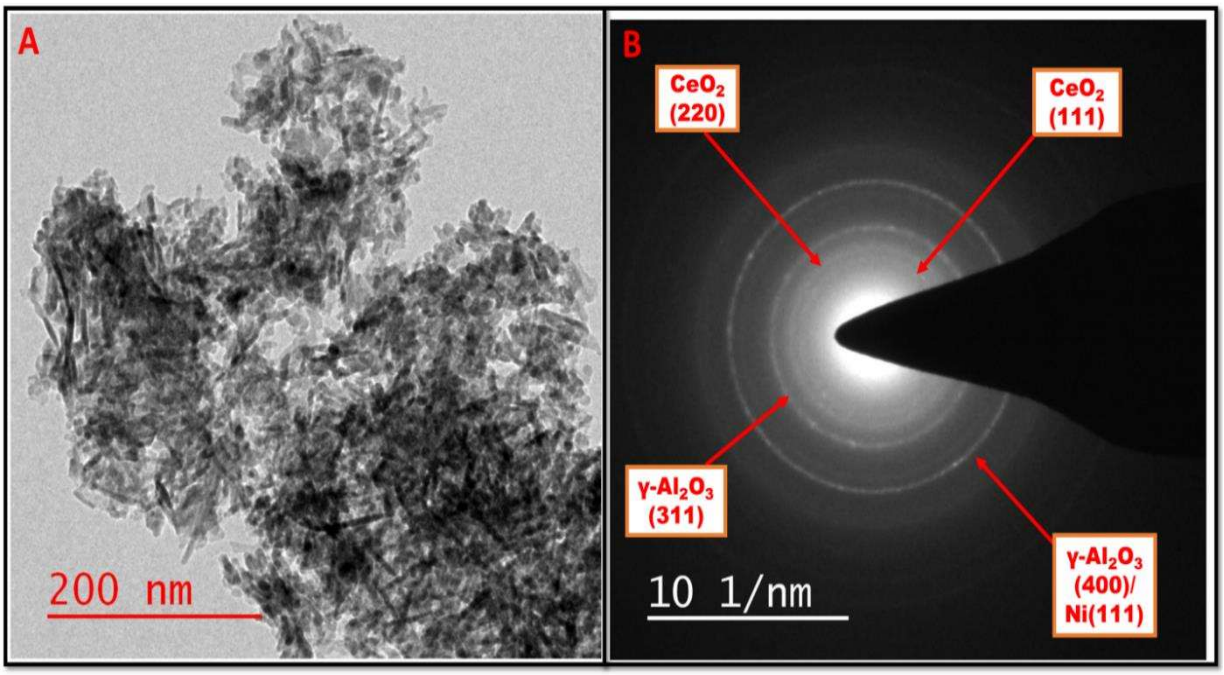

Fig. 4.7. TEM images and SAED diffraction of catalyst 2

Based on the analysis, the particles' size is approximately between the 12-20 nm range. However, despite having large crystallite sizes of Ni in catalyst 2, it showed better catalytic activity because it consisted of better dispersion on porous ALC support. The selected area

electron diffraction (SAED) patterns for both the catalysts indicated clean and strong ring pattern which indicates characteristics of polycrystalline nature and rings analysis represent the planes of γ-Al_2O_3 (400, 311) and CeO_2 (111, 200) with crystalline structure matched with the corresponding *hkl* planes from XRD analysis. Diffraction rings of Ni could not be detected in the case of catalyst 1. It may be because of the high dispersion of Ni in the size range of nanoparticles. However, for catalyst 2, the ring (corresponding to the d value 2.02 Å) could not be ubiquitously assigned to either γ-Al_2O_3 (400) with d value 2.0361 Å or Ni (111) with d value 1.981 Å. However, both the peaks corresponding to γ-Al_2O_3 (400) and Ni (111) were observed in XRD analysis.

4.6. Scanning Electron Micrograph

SEM–EDAX analysis was performed on the catalysts to find out the textural morphology of the catalysts, and the results are shown in **Fig. 4.8.**

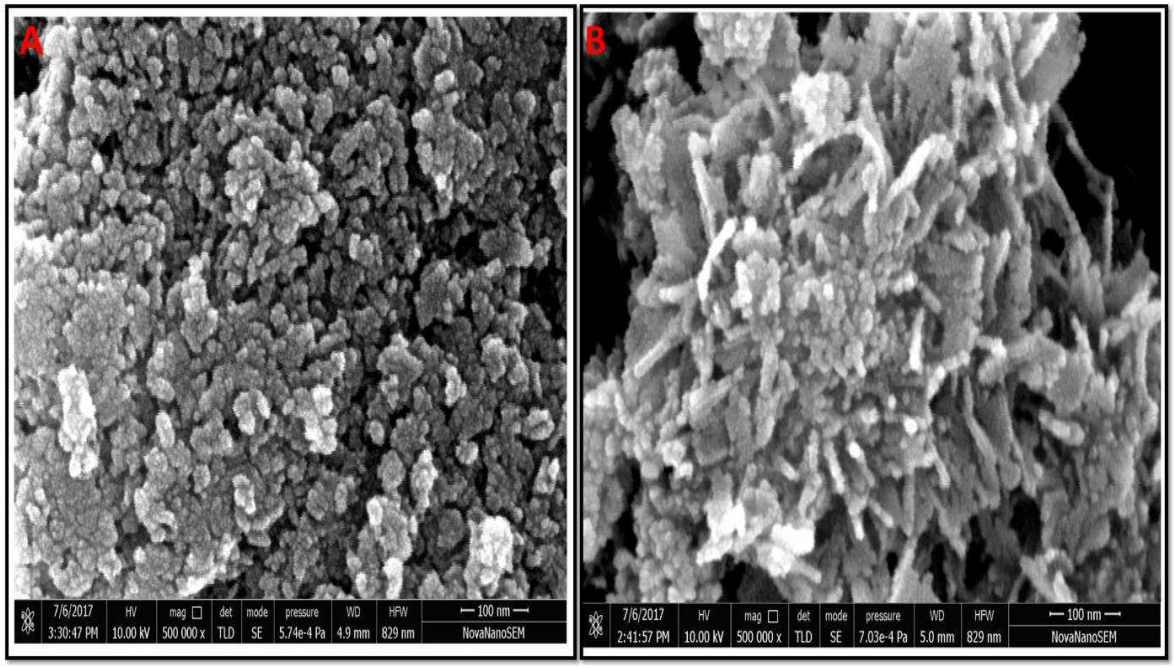

Fig. 4.8. SEM analysis of Catalyst 1 and Catalyst 2

In catalyst 2, the morphology of particles observed rod-like shape while catalyst 1 showed small dispersed particles and observed in a high cluster density group and agglomerated. Results of EDAX analysis of both the catalysts are shown in Fig. 4.9 and 4.10.

Fig. 4.9. SEM EDAX analysis of Catalyst 1

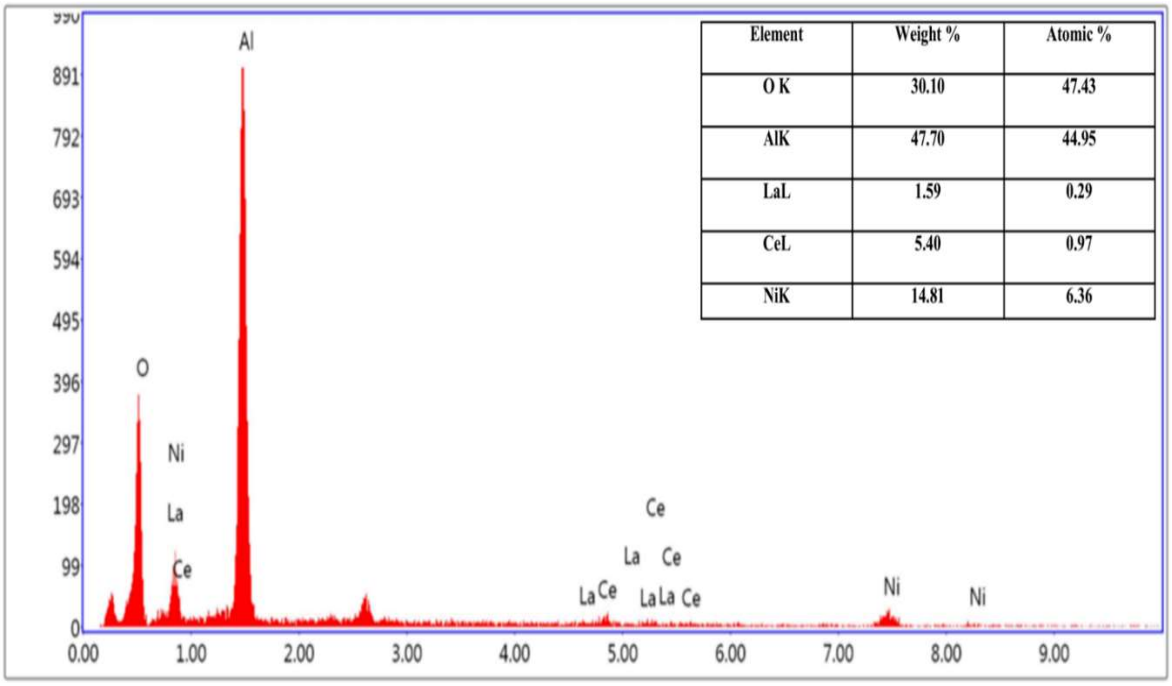

Element	Weight %	Atomic %
O K	30.10	47.43
AlK	47.70	44.95
LaL	1.59	0.29
CeL	5.40	0.97
NiK	14.81	6.36

Fig. 4.10. SEM EDAX analysis of Catalyst 2

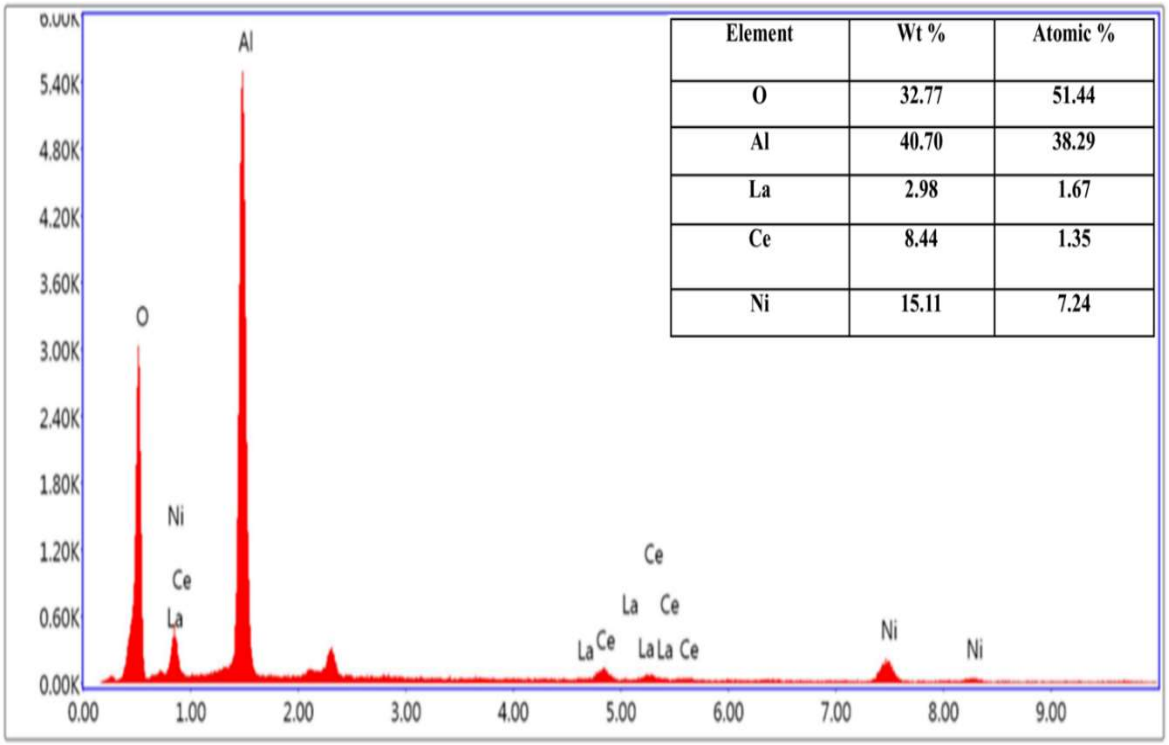

Element	Wt %	Atomic %
O	32.77	51.44
Al	40.70	38.29
La	2.98	1.67
Ce	8.44	1.35
Ni	15.11	7.24

During calcination, all ligands and associated coordinated ions were removed in the presence of an inert atmosphere from the synthesized nickel complex supported catalyst and $Ni(HCOO)_2.2H_2O$ supported catalyst.

4.7. X-ray photoelectron spectroscopy (XPS) studies of the catalysts

X-ray photoelectron spectroscopy analysis was carried out to investigate the oxidation state of chemical species and surface composition of the elements present on the surface of the catalysts. The subtraction of peak carried out by Shirley type background across all the spectrum and the intensities of each peak were evaluated by integral calculation. The fitting and deconvolution of peaks were performed by using Lorentzian - Gaussian method [289]. Binding energies were calibrated with taking reference to carbon (C1s) binding energy at 284.6 eV. In both the catalysts, the binding energies spectra of nickel and its characteristic peaks were observed between 845-880 eV. The spectra of Ni 2p peak for both the catalysts overlapped with the La3d, Ce3d peaks spectrum became uncertain about deconvoluting and hard to quantify due to complex characteristics of peaks spectrum. Mostly, the main uncertainty encountered as a result of the overlapping of Ni $2p_{3/2}$ and La $3d_{3/2}$. However, the XPS spectrum peaks of La were observed in La (III) species at binding energy 855.3 and 835.5 eV, respectively. To understand the effect of cerium on the support surface as oxygen storage and releasing agent, a detailed study of cerium spectra, as shown in

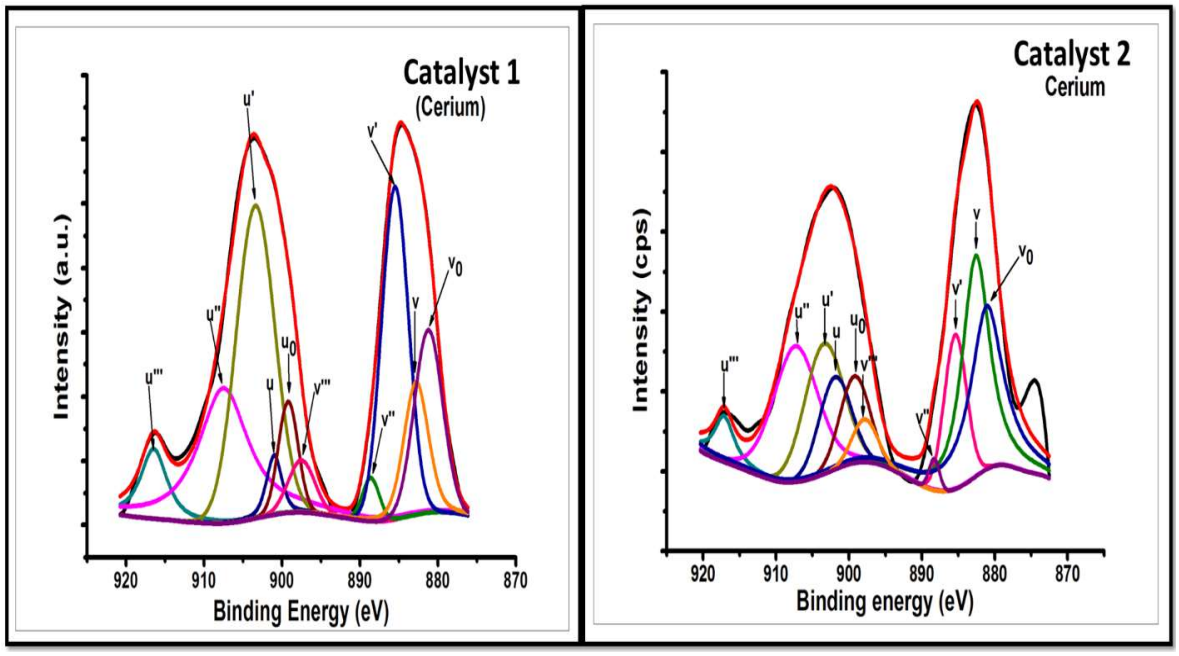

Fig. 4.11 (A) Ce 3d XPS spectra of catalyst 1 & **(B)** catalyst 2

Fig. 4.11 was carried out. XPS spectra of Ce3d are complex because the formation of different compositions is present in Ce^{3+} and Ce^{4+} species after deconvolution. The Ce3d core level showed multiple spin-orbital splitting corresponding to the $Ce3d_{5/2}$ and $Ce3d_{3/2}$ core species in the form of (u and v) summarized in Tables 4.3 4.5, respectively. It is reported that XPS spectra of Ce3d core levels were formed of 10 different states of various spin-orbit doublets corresponding to different states of Ce^{3+} and Ce^{4+} on the surface of catalysts [271, 290, 291]. The spectra of Ce3d peaks deconvoluted in split doublets (u'-v', u_0-v_0) are assigned to the Ce^{3+} species are given in **Tables 4.3 & 4.4.** It is observed from the result that the binding energy of Ce3d spectrum spits into the co-existence of Ce^{3+} and Ce^{4+} oxidation states and is much more complicated. Both Ce^{3+} and Ce^{4+} are composed of five doublets (u_0, v_0), (u', v'), (u''', v'''), (u'', v'') and (u, v) or in 10 peaks leveled as U and V corresponding to the spin-orbit splitting of $Ce3d_{5/2}$ and $Ce3_{d/2}$ components (see Fig 4.11 A and 4.11 B).

Table 4.3. Binding Energy (eV) (catalyst 1)

Binding Energies (eV)	Ce species	Peak assignment	Relative area (%)	Area
881.1	Ce^{3+}	v_0	22.46	28116.59
882.6	Ce^{4+}	v	14.13	17688.2
885.4	Ce^{3+}	v'	9.93	12427.8
888.3	Ce^{4+}	v''	0.95	1186.80
897.8	Ce^{4+}	v'''	1.86	2330.97
899.2	Ce^{3+}	u_0	4.45	5573.99
901.8	Ce^{4+}	u	8.50	10644.67
903.4	Ce^{3+}	u'	14.64	18323.38
907.3	Ce^{4+}	u''	19.05	23845.65
917.0	Ce^{4+}	u'''	4.01	5020.11

The results are also validated with the published results [223, 292]. The deconvoluted spectra ascertain that the peak of Ce^{3+} state (v_0, v', u_0 and u') are stronger in comparison to the Ce^{4+} states (v, v", v"', u, and u"). The synthesized catalysts showed stronger content of Ce^{3+} species, clearly attributed to the more significant amount of oxygen vacancies available in the CeO_2 lattice. The CeO_2 provides mobilizable oxygen vacancies, which is useful for preventing coke formation over the catalyst surface. Mobilizable oxygen was transferred from oxygen vacancies in the CeO_2 lattice to accelerate the carbon precursor's oxidation deposited over the catalyst surface. Hence, it is assumed that the catalysts having large amounts of Ce^{3+} species considered to be formed more oxygen vacancies. To evaluate the total fraction or relative amount of Ce^{3+} species present on catalyst surface sample (also allude as degree of reduction) was calculated in reference with a total area of cerium species. To obtain a precise analysis of the total amount of the CeO_2 and the contribution of the spectrum from the Ce^{3+} and Ce^{4+} can be determined from the following equations **(Eq. 2. & Eq. 3.)** [293].

$$Ce^{3+} = u' + u_0 + v' + v_0 \quad (2)$$

$$Ce^{4+} = u''' + u'' + u + v''' + v'' + v \quad (3)$$

$$Ce3+(\%) = \frac{Ce3+}{Ce4+ + Ce3+} \quad (4)$$

The concentration of Ce^{3+} and Ce^{4+} in CeO_2 can be estimated through **Eq. 2. & Eq. 3.** The concentration of Ce^{3+} in CeO_2 over both the catalyst was found to be around 51.34 % and 58.37% for catalyst 1 and catalyst 2, respectively, calculated from **Eq.4.** It is noticed from Ce^{3+} calculation catalyst synthesized from MOF derive nickel complex showed more amount of Ce^{3+} species due to that more vacancies of oxygen are present in the catalyst. Consequently, catalyst 2 showed better catalytic activity and stable behavior towards coke deposition.

Table 4.4. Binding Energy (eV) (Catalyst 2)

Binding Energies (eV)	Ce species	Peak assignment	Relative area (%)	Area
881.2	Ce^{3+}	v_0	10.18	6497.85
882.8	Ce^{4+}	v	7.06	4501.49
885.5	Ce^{3+}	v'	17.42	11112.51
888.6	Ce^{4+}	v''	1.50	956.84
897.5	Ce^{4+}	v'''	2.72	1737.75
899.2	Ce^{3+}	u_0	7.24	4620.35
901.0	Ce^{4+}	u	3.63	2319.54
903.4	Ce^{3+}	u'	23.52	15001.92
907.5	Ce^{4+}	u''	18.37	11720.42
916.5	Ce^{4+}	u'''	8.34	5318.40

4.8 Catalytic activity and yield of catalysts

Acetic acid conversions at different temperatures are displayed in **Fig. 4.12 & 4.13 A** for both the prepared catalysts and bare support. Due to the steam reforming reaction's endothermic nature, the conversion of acetic acid over both the catalysts and over-the-prepared support increases with increasing temperature. Thermodynamically, in all aspects, the distribution of evolved hydrogen increases with increasing temperature whereas, the methane content decreases to arrive at a maximum. This is due to the promotion of steam reforming reaction as temperature increases because it is an endothermic reaction since water-gas shift is an exothermal reaction, the CO mol % increases at the expense of CO_2 as the temperature increases (**4.13 C**), also consuming H_2 (reverse reaction). At the same time, methanation reactions are prevented, as both are highly exothermic reactions. This further leads to a decrease in H_2 content at high temperatures, at which methanation is almost completely unfavoured (CH_4 content below 0.2 mol %) (**4.13 D**). In ALC support (**Fig. 4.12**), AcOH does not completely convert even at high temperatures. It showed remarkable

activity for the conversion of AcOH; however, it gives lower activity in terms of steam reforming and produces much less yield towards H_2 and CO_2. The main products obtained in the gaseous phase at higher temperatures are H_2, CO, CH_4, CO_2 resulting from the thermal decomposition of the acetic acid, and acetone is the main product at lower temperatures produced via ketonization reaction. The yield of acetone decreased with an increase in reaction temperatures and C1 products developments due to C-C bond cleavage. This result inferred that only ALC support favors the ketonization reaction at lower temperatures, whereas C-C bond cleavage favors at elevated temperatures. The reforming activity becomes appreciably higher in the case of when Ni was loaded over the support. Almost complete conversion of acetic acid and high H_2 yield obtained at temperature 600 ºC (**4.13 B**). Without active metal catalysts on the support, only decomposition reaction is prominent for acetic acid conversion, and only marginal steam reforming activity might have occurred over the support surface.

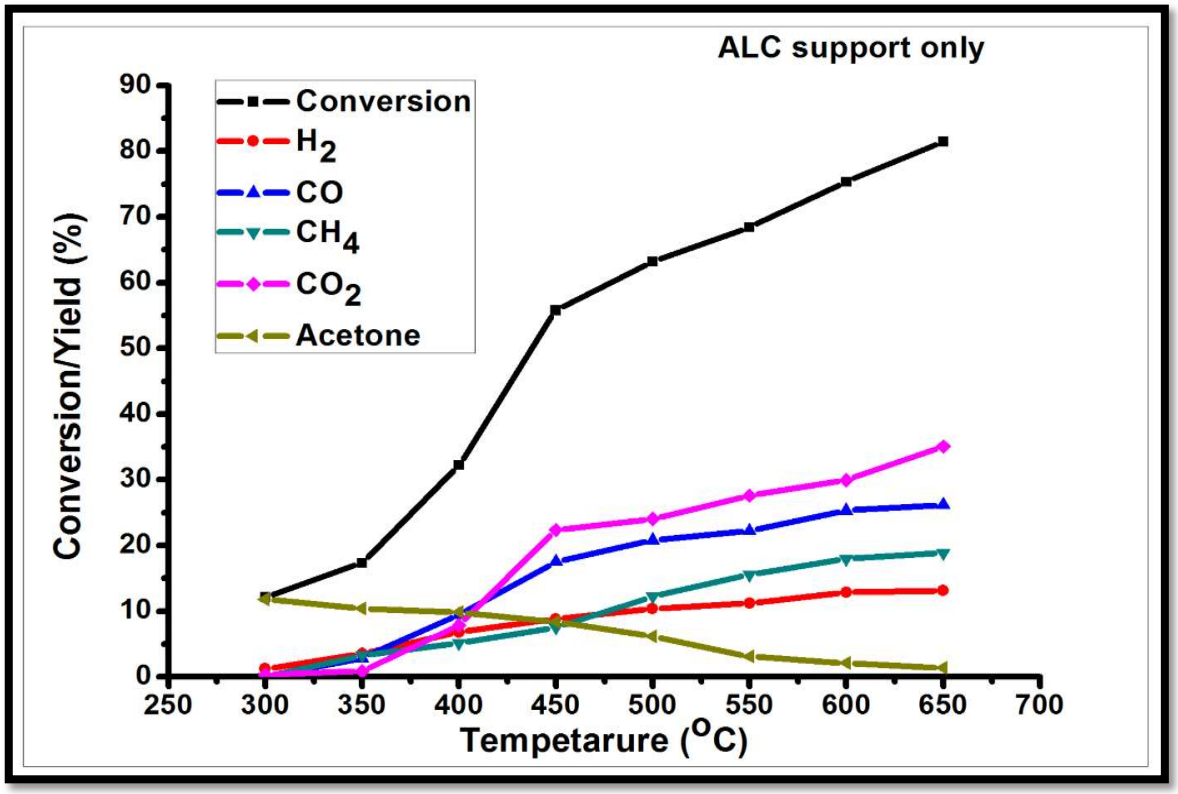

Fig. 4.12. Conversion of AcOH and product distribution as a function of temperature over ALC support

During AASR in the studied temperatures range, the main out products were H_2 and CO_2 with small amounts of CO and CH_4 were the major outcomes in both Catalyst 1 and 1Catlyst 2. Whereas CH_4, CO_2, and acetone were the major outcomes over prepared support only. A small amount of CH_4 was generated over both supported nickel catalysts, but the yield of CO is high over catalyst 1 at higher temperatures (**4.13 C**).

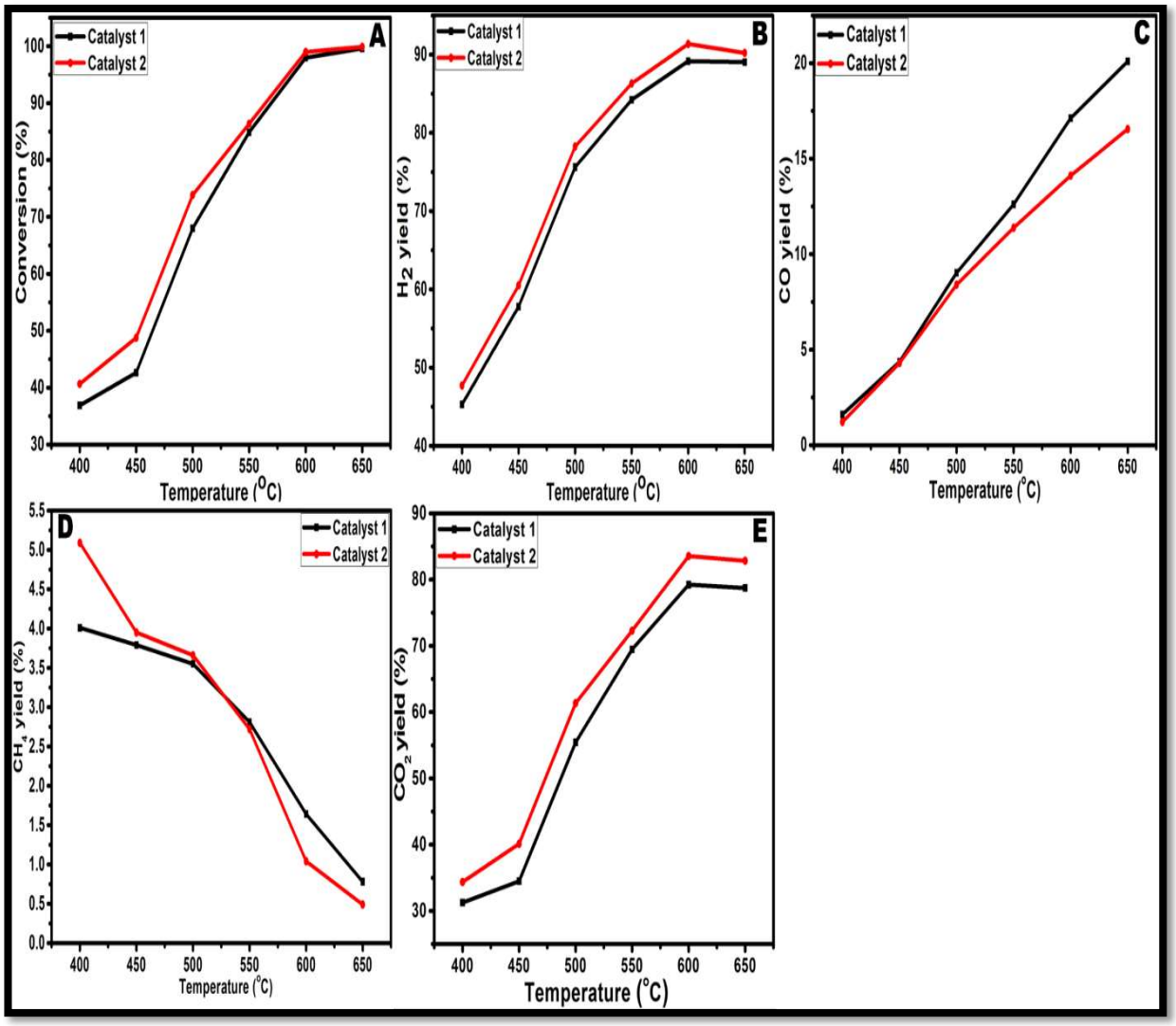

Fig. 4.13 (A)-(E). Conversion of acetic acid and yield of the gaseous products over catalyst 1 and catalyst 2 in the different temperature range of 400 - 650 °C. Experimental conditions: S/C mole ratio 6.5:1, mixture flow rate 2.5 mL/h

Whereas the yield of CO_2 and H_2 is more in the case of catalyst 2 than catalyst 1 (**4.13 B & E**). The results also described that no ethylene formation was observed due to rapid

decomposition as it was produced. Catalytic activity due to homogeneous reaction and quartz wool was considered negligible during the reforming reaction. As displayed in **Fig. 4.13 (A),** both catalysts produce approximately 100% conversion of acetic acid at 650 ºC and S/C molar ratio of 6.5. The high yield of CO_2 suggests the contribution of water gas shift reaction to a great extent. As shown in **Fig 4.13 B. & E.**, the dominance of H_2 and CO_2 at high temperatures during reaction indicated that the main reactions are steam reforming and water-gas shift (WGS). Other intermediates like CO are generated via decomposition and reverse water gas shift reaction at higher temperatures.

4.9. Stability Test

The stability of both catalysts was evaluated with more than 36 h time on stream (TOS). Stability testing for both catalysts was performed at temperature 600 ºC, keeping with the same operating conditions for 36 h; results are shown in **Fig. 4.14.**

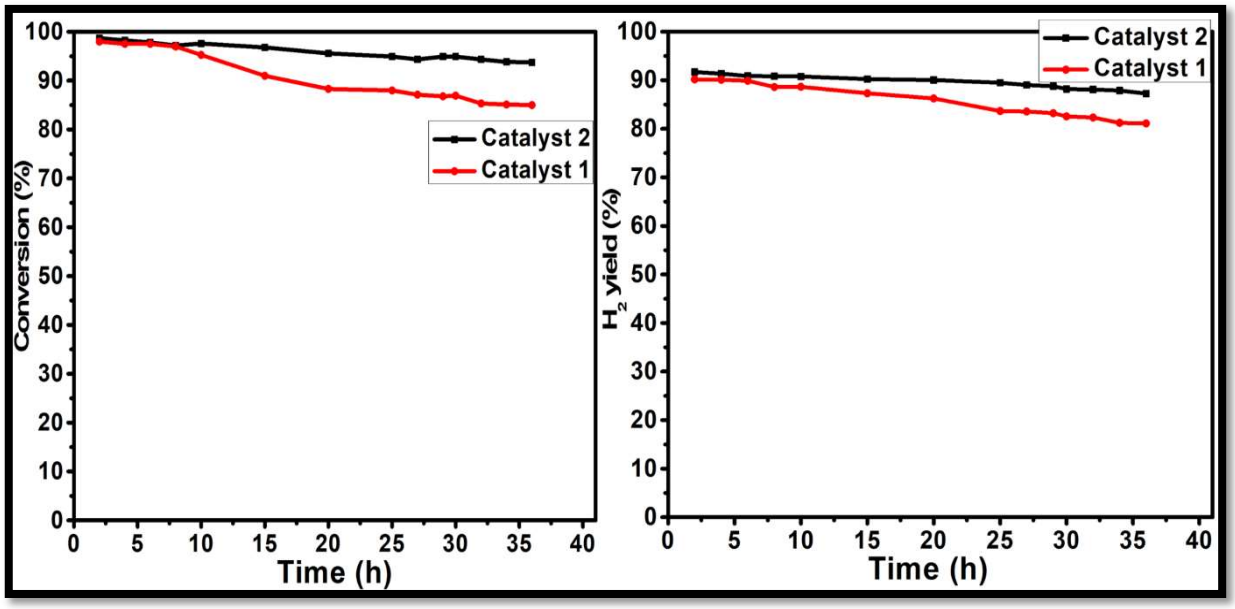

Fig. 4.14. Conversion and H_2 yield (%) of catalyst 1 and catalyst 2, Reaction condition: temperature - 600 ºC; N_2 flow rate - 30 mL/min; mixture flow rate -2.5 mL/h; and S/C-6 mol/mol

Catalyst 2 showed stable behavior in terms of conversion as well as H_2 yield in comparison to catalyst 1. The better activity and yields for H_2 are due to MOF-derived nano-nickel particles form a porous three-dimensional framework, and available high surface area of

the catalyst and the availability of a large number of free nickel particles and more Ce^{3+} vacancies on the support surface resulting in high catalytic activity and stability. The conversion and H_2 yield of catalyst 1 retain approximately the same during 10 h but showed a decreasing trend in the conversion and H_2 yield. While Catalyst 2 exhibited better stable behavior for coke deposition of more than 36 h. The long stable behavior of catalysts could be related to Ce and La promotion, which hinders coke formation. The decline in conversion and H_2 yield with time on steam for both the catalysts related to the coke deposition over the catalyst surface. The carbon deposition mainly occurred via thermal decomposition and the reaction intermediates generated during the AASR [33].

4.10. DT-TGA analysis of spent catalysts

DT-TGA analyses were carried out in oxygen after the stability test to determine the presence and type of carbonaceous species formed on the catalyst's surface. **Fig. 4.15 (a)**

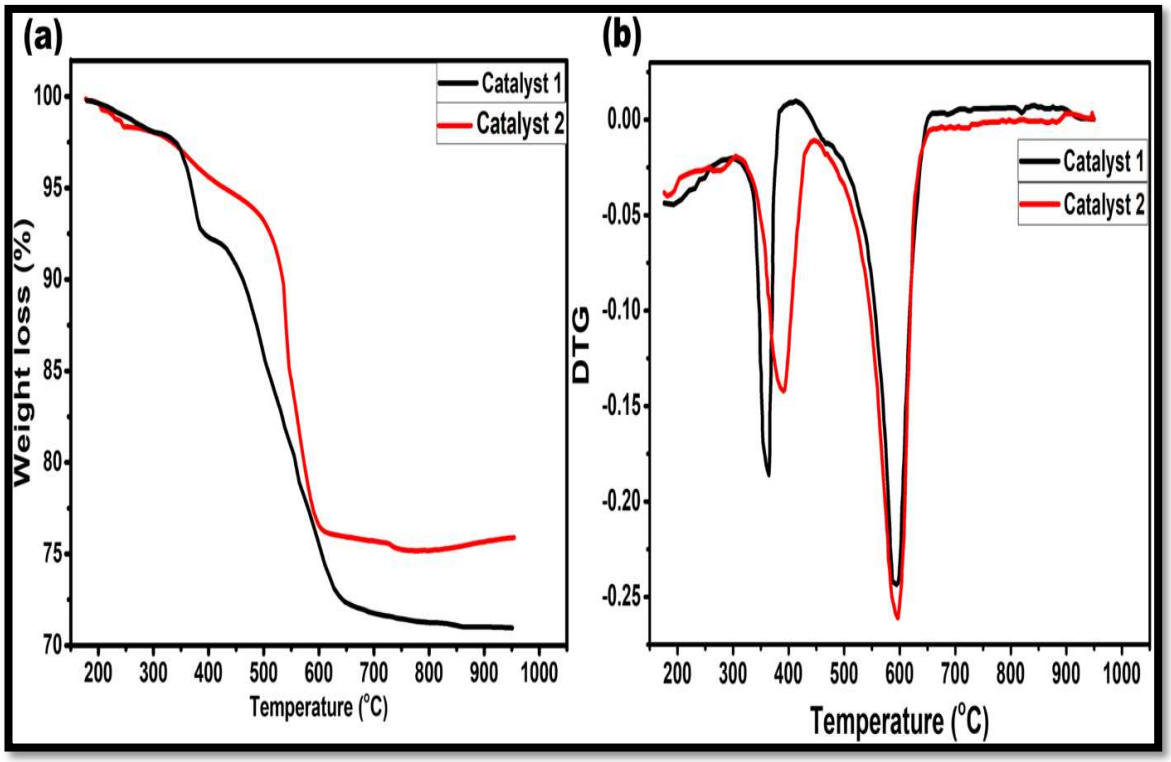

Fig. 4.15. TGA-DTG profile of spent catalysts after stability test (a) TG (b) DTG

shows the weight losses due to the combustion of deposited coke corresponding to catalyst 1 and catalyst 2, which were 29.0 and 24.1%, respectively. The amount of coke deposited on catalysts 1 was slightly higher than catalyst 2 due to less catalytic activity. The results indicated that coke formed over the catalyst depends on Ni quality present at the catalysts' surface and its distribution. Moreover, the low surface area suffers more coke deposition. As displayed in **Fig. 4.15 (b),** two distinct peaks, first at temperatures in the region of 350-400 °C and the second in the 550-600 °C region, were observed. It indicates the presence of two different carbonaceous species (amorphous and filamentous). The first peak was attributed to coke containing species like CH_x and C* (surface carbon) due to catalytic cracking reactions termed as amorphous coke, [242] and second peaks assigned due to polymerization of organics on catalyst surface termed as polymeric/filamentous coke, especially on the surface of support [294]. Wang et al. also investigated the AASR over the Ni-based catalyst and reported that adsorbed coke precursor CH_x*(x=1-3) formed due to catalytic reactions are responsible for coke deposition[295]. Furthermore, it was also reported that at lower temperatures, coke deposition was favored significantly via the "Boudouard reaction." However, at elevated temperatures, CH_4 cracking and other intermediates formed via AcOH decomposition forming carbonaceous species (CH_x*), which further responsible for coke deposition [138].

Summary

The γ-Al_2O_3 support incorporated with La_2O_3-CeO_2 prepared via two different methods was investigated in acetic acid steam reforming for hydrogen production. The incorporation of La_2O_3-CeO_2 in γ-Al_2O_3 enhances catalyst stability by preventing the rate of carbon deposition and the sintering process. From the results, we could infer that both catalysts over modified ALC support exhibited approximately 100% conversion and high H_2 yield without much deactivation because of the incorporation of modified support over 36h TOS.

AASR and reverse water gas shift (RWGS) were the major reactions that govern the outlet gas distributions at high temperatures. However, catalyst 2 showed better results in terms of H_2 yield in comparison to catalyst 1 catalyst. Moreover, it's also found much stable nature up to 36 h towards coke deposition. In addition, catalyst 2 exhibited a slightly higher surface area and larger pore sizes due to the regular arranged ordered pore size and porosity and coordinate bonding of catalyst, which improved the reactant's movement and catalytic activity.

Moreover, it observed a large number of free nickel particles and more Ce^{3+} vacancies on the support surface resulting in high catalytic activity and stability. Amorphous-like carbon and filamentous-like carbon were observed over spent catalysts after the stability test. Therefore, catalyst 2 showed better catalytic activity since it showed less coke deposition and a high H_2 yield.

II

Section: II

Effect of Ni loading on catalytic activity and products distribution for acetic acid steam reforming over nickel-based catalyst synthesized via MOF process

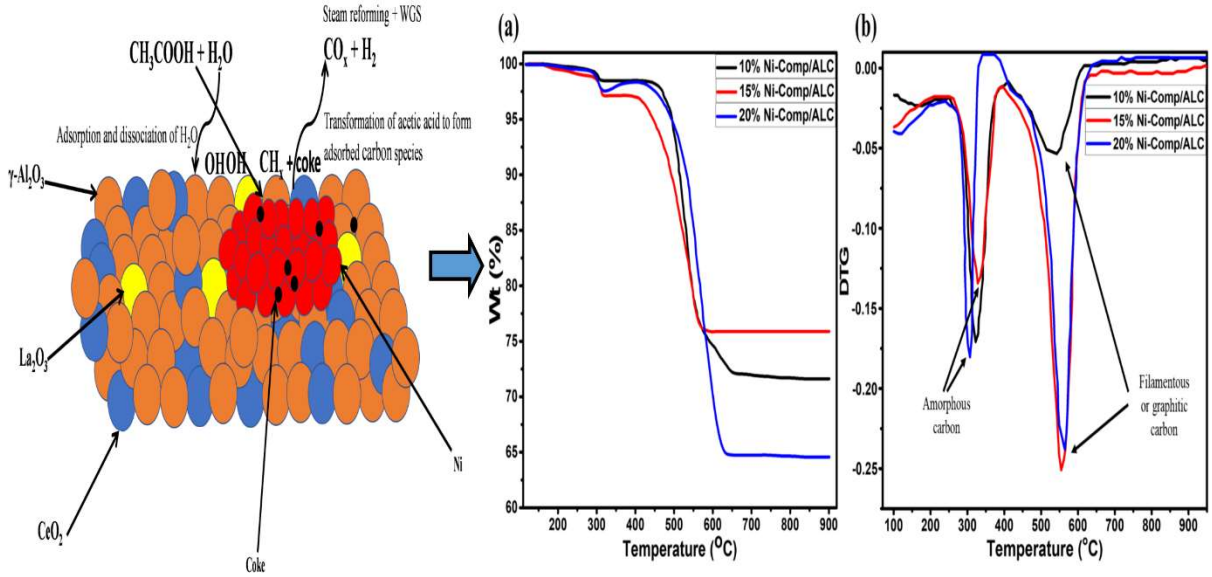

Our previous section reported that using impregnation of MOFs derived Ni precursor over ALC support showed excellent catalytic activity and stability for AASR than nickel formate precursor, and different types of nickel precursors on ALC showed different interaction with the support. Ni and the support interaction played an important role in better catalytic performance. It has also observed that MOF-derived Ni catalyst possesses a relatively large number of free nickel particles and more numbers of Ce^{3+} vacancies on the support surface compared to commercial nickel precursors. For all these reasons, it showed higher catalytic activity and stability for the AASR.

Herein, in the present work, we have focused on investigating the correlation and ineraction effect of Ni content (x% Ni, x = 0, 10, 15, and 20 wt%) with properties on the catalytic performance of an alumina-lanthanum-cerium (ALC) supported MOF-derived Ni catalyst for AcOH steam reforming to maximize H_2 yield. The content of Ni in the Ni/ALC catalyst was adjusted by controlling the composition of its precursor (metal-organic framework (MOF): (Ni $[(bpy)_2]Cl_2).6H_2O$)). As a result, catalysts were designated as catalyst 2 (15 wt% Ni), catalyst 3 (10 wt % Ni) and catalyst 4 (20wt % Ni). On the other hand, higher Ni loadings (> 15 wt.%) were less advantageous for the AASR reaction (in terms of activity and stability) due to an increase in particle size of Ni and/or decrease in its dispersion. On the whole, the present study is expected to offer valuable insights into the utilization of MOF-based catalysts for H_2 production through the AASR reaction.

5.1 Catalysts Characterization

5.1.1. XRD analysis of catalyst

The XRD patterns of Al_2O_3, ALC, and Ni-comp/ALC(at Ni = 10, 15, and 20 wt.%) catalysts are presented in Fig. 5.1. As it can be seen, the scattering diffraction peaks of- γ-Al_2O_3 (at 2θ = 37.2°, 45.8°, and 66.7°; JCPDS 86-1410), the cubic Ni phase (2θ = 44.5° (111), 51.8°

(200), and 76.4° (220)), and cubic fluorite crystal structure of CeO_2 (2θ =28.30º (111), 33.13º (200), and 56.33º (311)) could be found overall Ni-comp/ALC catalysts.

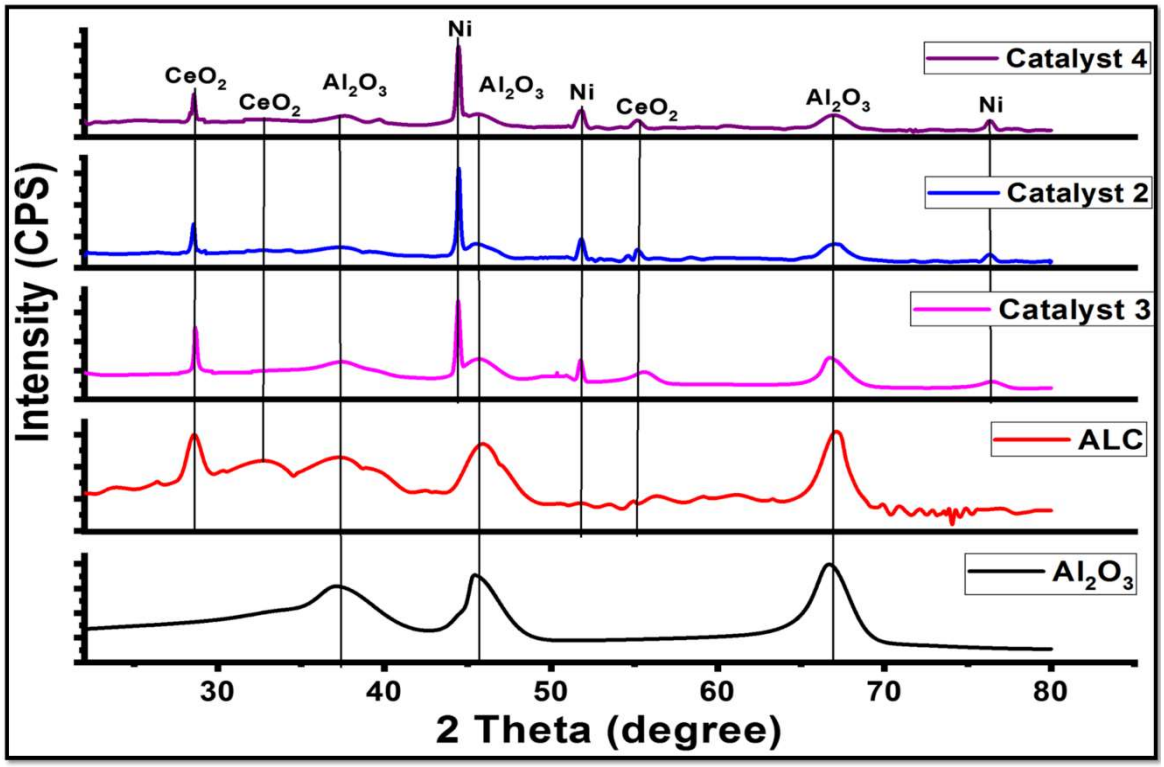

Fig 5.1. XRD patterns of catalyst 2, 3 and 4

The characteristic diffraction peaks of the cubic fluorite crystal structure of CeO_2 were observed in ALC support [1]. The absence of the characteristic nickel (II) oxide (NiO) peaks (2θ = 37.3º and 43.3º) from any of the catalyst samples indicates that the MOF Ni precursor exclusively provides metallic Ni sites after calcining in inert atmosphere on the catalyst surface. The detailed decomposition analysis of MOF Ni ($Ni[(bpy)_2]Cl_2$) precursor via DT-TGA was reported in chapter 3. Table 5.1 summarizes the crystallite sizes of the metallic Ni particles based on the XRD diffractograms using the Scherrer equation. Notably, the estimated crystallite size of metallic Ni particles increased with increasing Ni loading, recording 32, 37, and 63 nm at 10, 15, and 20% Ni-comp/ALC catalyst, respectively. Ni crystals observed in catalyst 4 were almost three times larger than that in catalyst 3. Such a difference in the Ni crystal size indicates the weak interaction between metal and support in catalyst 2 to make it vulnerable towards sintering [2]. Further, such

weak interactions may promote the reduction of nickel oxides [3]. The crystal size of metallic Ni in the 10% Ni-comp/ALC samples was observed to be approximately 32 nm, while that in 15 wt% only marginally increased to 37 nm. In contrast, a further increase in the Ni loading to 20 wt% significantly increased its size to 63 nm. Such a sharp rise can be explained by the agglomeration of Ni particles through the blocking of the smaller pores with the reduction in surface area.

5.1.2 Surface area and pore size analysis

The N_2 adsorption-desorption isotherms of all selected materials are provided in Fig. 2. The obtained isotherms demonstrated a typical Langmuir type IV behavior, commonly observed from mesoporous materials in a size range of 2-50 nm. In addition, the decreases in hysteresis loop height with increasing Ni loading indicate the lowering of surface area and total pore volume (Table 5.1).

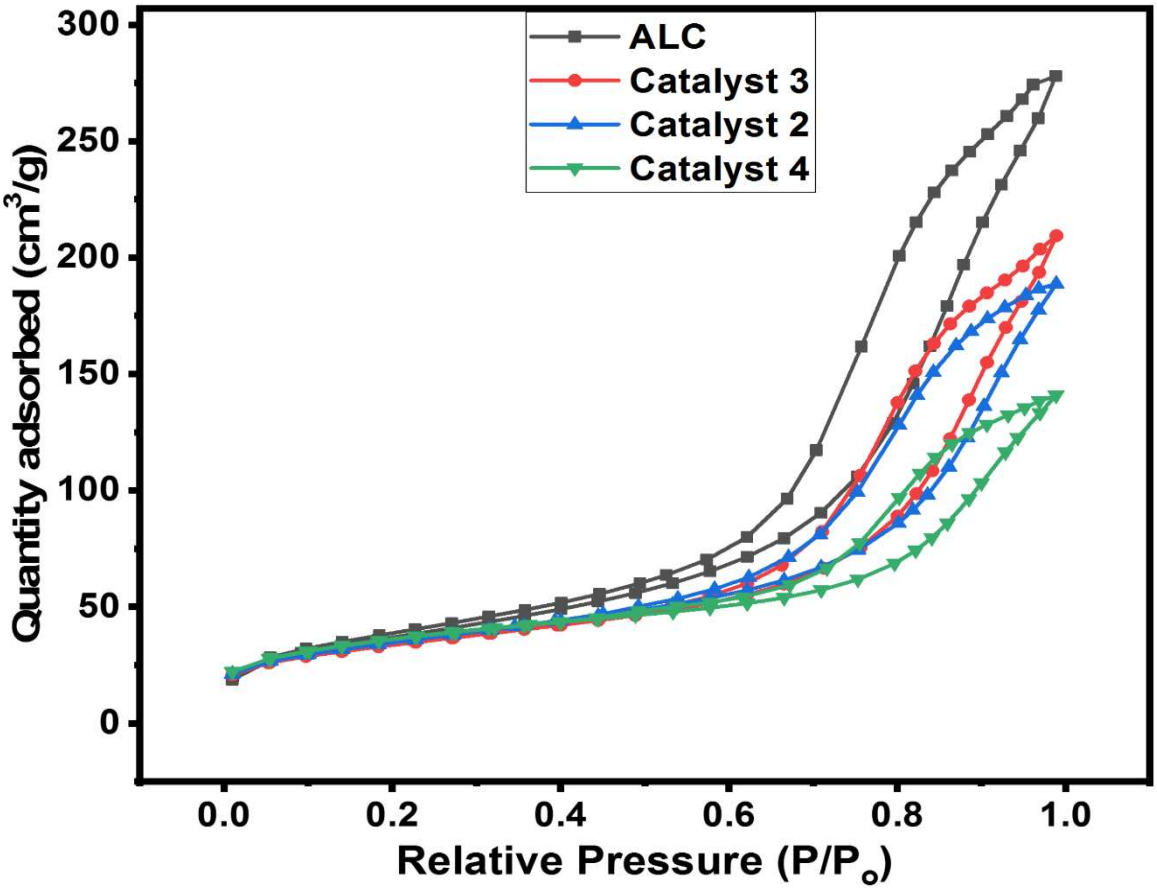

Fig. 5.2. N_2 adsorption-desorption isotherms of the support and catalysts

The pore volume decreased from 0.43 cm^3 g^{-1} in support to 0.31 cm^3 g^{-1} in catalyst 2. However, further increment in the Ni loading did not decrease the total pore volume significantly. As shown in Table 5.2, both the support and catalyst samples possess the majority of pores in the < 20 nm diameter size range. An increment of the Ni loading resulted in the corresponding decline of pores with < 20 Å diameter sizes. The Ni crystallites might likely have blocked a fraction of smaller-sized pores. Information on the BET surface area, average pore volume, and pore size of catalysts is listed in Table 1**.** The addition of Ni progressively lowered the surface area from 133 m^2 g^{-1} (ALC) to 110 m^2 g^{-1} (catalyst 4). Crystallite size of metallic nickel calculated through Scherrer calculation in 10 wt% Ni loading was observed around 32 nm. The increase of Ni loading 10 to 15 wt% on the support showed the only marginal difference in crystallite size from 32 to 37 nm. While a further increase of Ni loading showed a significant rise to 63 nm, it might be due to the agglomeration of nickel particles that blocked the smaller pores and reduced the surface area.

Table 5.1. Textural properties of synthesized catalysts

Support/Catalyst	Surface area (m^2/g)	Total pore Volume (cm^3/g)	Average pore size (nm)	Crystal size of Ni[a] (nm)
γ-Al_2O_3	169	0.61	9	-
Al_2O_3-La_2O_3-CeO_2 (ALC)	133	0.43	8	-
Catalyst 3	122	0.31	9	32
Catalyst 2	120	0.29	8	37
Catalyst 4	110	0.28	10	63

[a](111) plane

Table 5.2. Pore size distribution of catalysts

Species	Pore size range (Å) and corresponding pore volume (cm^3/g)			
	0≤dp≤20	20≤dp≤40	40≤dp≤60	60≤dp≤80
$Al_2O_3/La_2O_3/CeO_2$ (ALC)	0.38	0.05	-	-
Catalyst 3	0.27	0.027	0.01	-
Catalyst 2	0.25	0.02	0.01	0.01
Catalyst 4	0.20	0.04	0.02	0.02

5.1.3. TPR analysis

The promotion of rare earth metals (La_2O_3 and CeO_2) into Al_2O_3 is expected to alter its electronic properties and the interaction with the active metallic Ni sites. Hence, Fig. 5.3 shows the TPR analysis of the as-prepared Ni-based catalysts at different Ni loadings. As shown in Fig. 5.3, all Ni-comp/ALC catalysts were able to be fully reduced in the 300 to 550°C temperature region with the principal reduction peaks situated at ca. 400 to 450°C, corresponding to the reduction of dispersed amorphous NiO [4]. The presence of the main reduction peak of unsupported NiO in this range also suggests the weak interactions between the ALC support and Ni species. The obtained TPR profiles also showed a minor shift in the peak position from 450 to 438 °C with increasing Ni loadings from 10 to 20% in the prepared Ni-comp/ALC catalysts due to decrease of metal-support interaction. The reduction behavior of the NiO/ALC catalyst has been well documented in the literature [5-7]. In general, the NiO particles strongly interact with γ-Al_2O_3 to form an amorphous nickel aluminate spinel-like structure. The reduction peak for such species is usually observed above 600 ºC [5-7]. Additionally, the reduction peak for bulk CeO_2 associated with Al_2O_3 and NiO is usually detected above 800°C [5]. However, in all of our catalyst samples, the

CeO_2 reduction peak was not observed to possibly reflect the formation of a solid solution involving Ni or La [7].

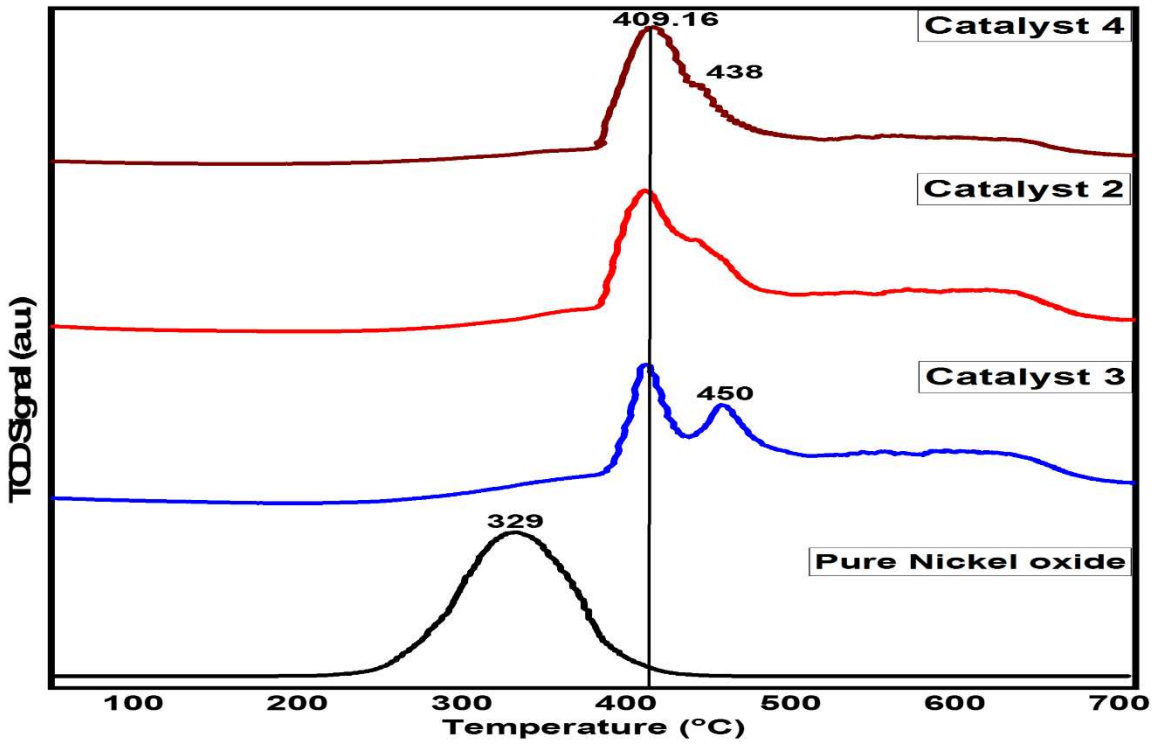

Fig 5.3. TPR analysis of Catalysts

The incorporation of Ni^{2+} or La^{3+} species over the CeO_2 lattice resulted in the replacement of Ce^{4+} ions to Ce^{3+} ions. Such a process can lead to the formation of a solid solution with the generation of oxygen vacancies (O_{vac}). Due to the presence of the solid solution phase, the CeO_2 reduction peak was shifted to a lower temperature to overlap with the peak for Ni^{2+} ions [8, 9]. Since the reduction of other oxides present in the catalysts requires higher temperatures, the observed reduction peaks in the TPR profile have been assigned to the reduction of nickel oxides only. As higher temperatures are required to reduce other oxides present (e.g., CeO_2) in the catalyst structure or strong interaction of Ni with alumina corresponding to spinel $NiAl_2O_4$. Therefore, the observed peaks in the TPR profile have been assigned to the reduction of weak to medium interacted NiO only. It was further observed from the TPR profiles that the reduction of NiO present in the catalyst samples requires higher temperatures than the unsupported NiO due to weak to medium interaction with the support. Therefore, the shift in NiO reduction peak

position to higher temperatures indicates the existence of weak to medium metal-support interactions. The metal-support interactions can be divided into weak and strong interactions, each requiring low and high-temperature conditions. The fraction of strongly interacted Ni is the highest in catalyst 3. Therefore, an increase in the Ni loading decreases the fraction of strongly interacted Ni species in the catalyst sample. Based on the TPR results, it can be concluded that the ALC support possesses two types of binding sites for the interaction with Ni species. Once the stronger Ni binding sites are fully occupied, the weaker binding sites begin to be filled with the increase of Ni loading.

5.1.4 SEM analysis

The morphology of the 3, 2, and 4 wt% Ni-comp/ALC catalysts was assessed by FE-SEM as presented in **Fig. 5.4.** For all the samples, uniform dispersion of metal was observed with spherical morphology for each of the three loadings.

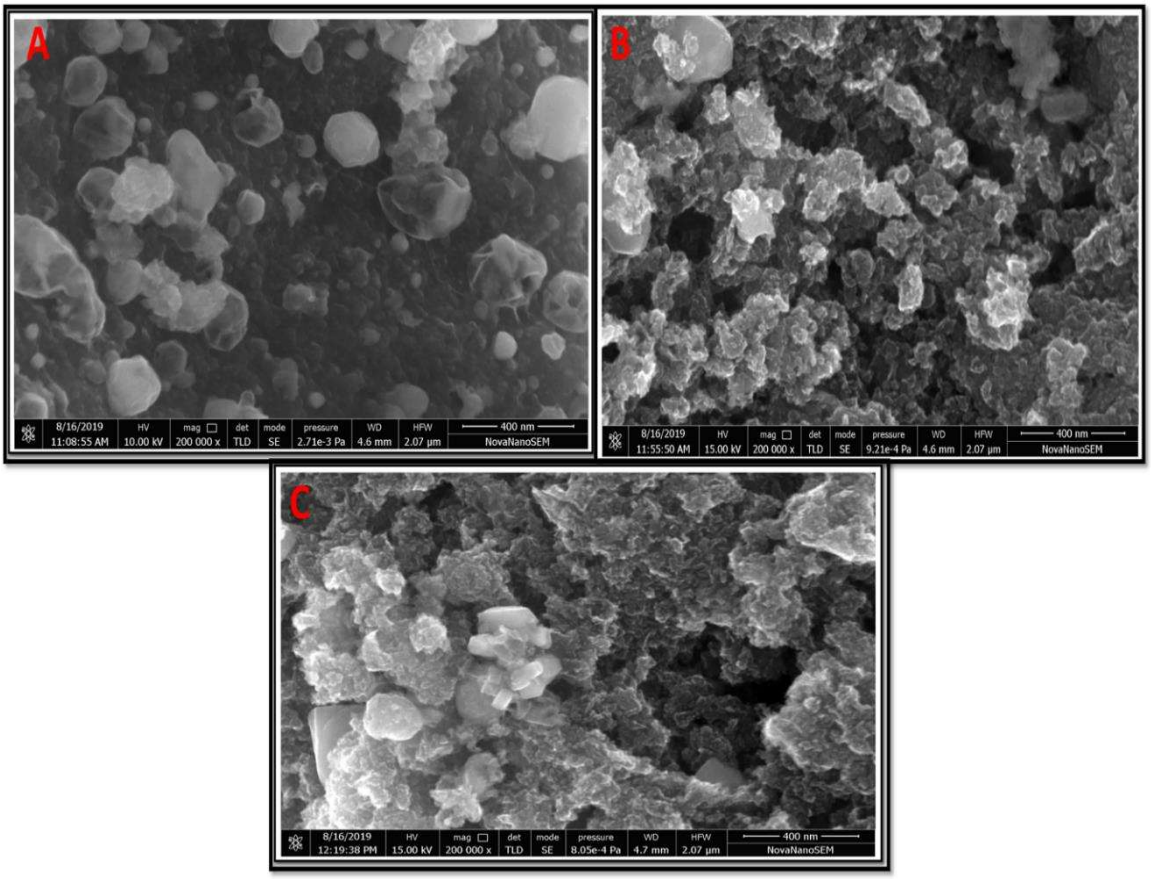

Fig. 5.4. (A) Catalyst 3 **(B)** Catalyst 2 **(C)** Catalyst 4

5.1. 5. TEM Analysis

TEM images of the catalysts 2, 3, 4 were obtained further to explore their structural information at an atomic scale (Fig 5.5 (A) – (C)). The TEM images revealed the cubic crystalline structure of Ni for all the analyzed catalyst samples. . All three catalysts displayed the agglomerated spots of dispersed Ni particles over the ALC support. The Al_2O_3 particles had rice grain-like morphology, with the Ni particles occurring as dark circles on their surfaces. The particle size of catalyst 3 sample was observed to be in the 15-20 nm range. The particle size was observed to increase with a rise in Ni loading (40-65 nm) (Fig. 5.5). Large-sized Ni particles (> 15wt.%) are not favorable for the AASR reaction as they accelerate coke deposition rate on the catalyst surface due to CO disproportion [10, 11].

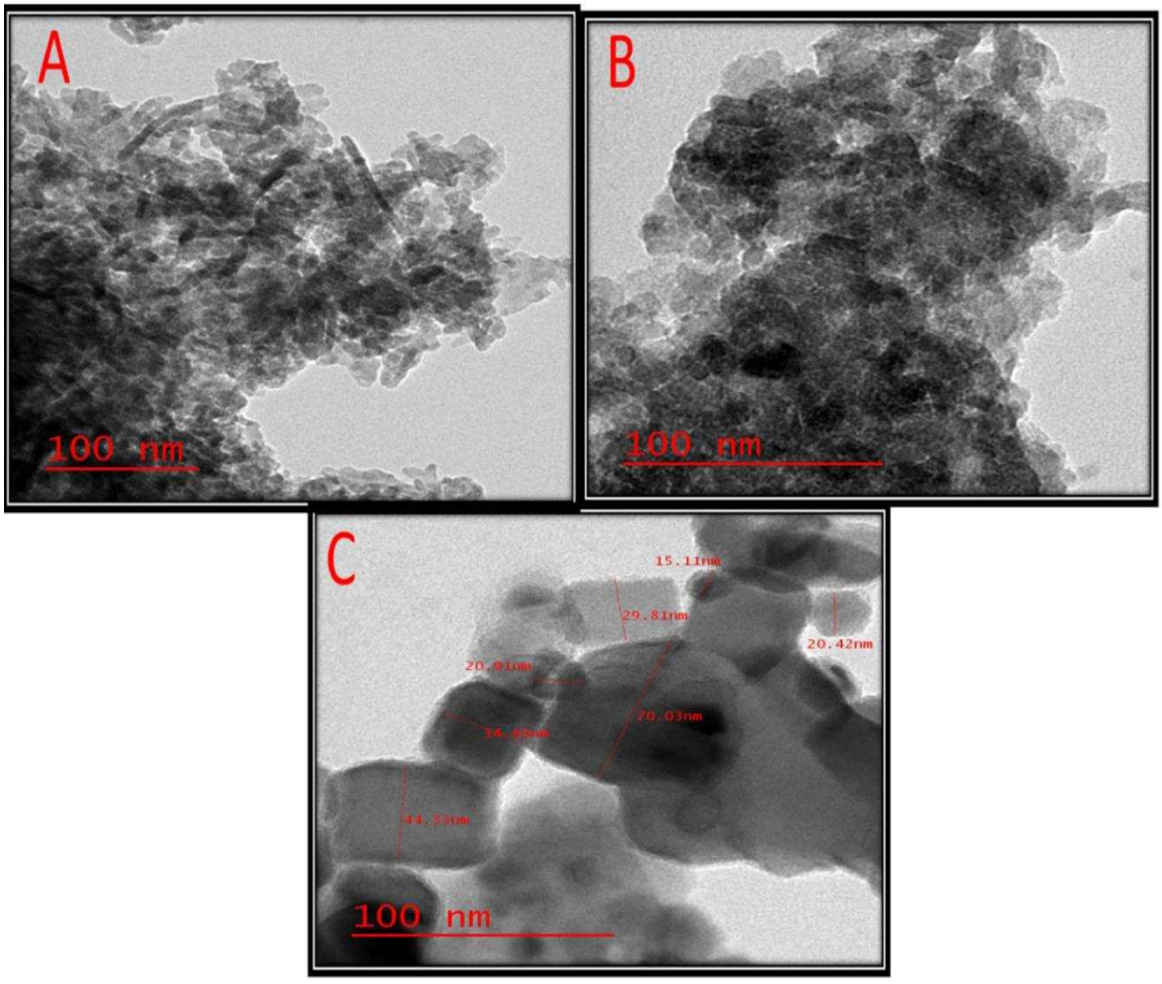

Fig. 5.5. TEM micrographs of **(A)** Catalyst 3 **(B)** Catalyst 2 **(C)** Catalyst 4

5.2. Effect of the operating variables on the performance of catalysts

5.2.1. Effect of Reaction Temperatures

The effect of reaction temperatures on the AcOH conversion and product yield has been elucidated in Fig. 5.6 (A)-(B). In these reactions, the steam to carbon molar ratio (S/C) ratio and the weight hourly space velocity (WHSV) values were fixed at 6.5 and 1.05 h^{-1}, respectively. As shown in Fig. 5.6, the bare ALC support did not show any catalytic activity even at elevated temperatures. On the other hand, the AcOH conversion efficiency and H_2/CO_2 yields over Ni-comp/ALC catalysts increased with increased AASR reaction temperature. Specifically, at elevated reaction temperatures above 500°C, AcOH was completely converted to H_2 and CO_2 as the primary products, with H_2/CO_2 yield of 1.09, indicating the dominated SR process onto all the Ni-comp/ALC catalysts. In contrast, at lower temperatures (400-500 ºC), higher yield of CH_4 (4-5%) was observed, possibly due to CO_2 methanation onto all tested catalysts [12]. However, CH_4 formation (0.15 to 0.4 %) reaches the minimum at elevated temperatures due to the suppression of methanation (as an exothermic reaction) and the promotion of the SR reaction of CH_4 generated [13]. As a fact, the active Ni phase can promote both the breakage of C-C and C-H bonds and the SR of CH_4 at elevated temperatures. Beyond 600°C, the H_2 yield dropped gradually from 91.36 % to 89.21%, while CO yield increased from 14.11 to 16.55 %, resulting from the promotion of reverse water gas shift reaction (RWGS). At 650 ºC, all the tested catalysts displayed the complete conversion of AcOH with varying product distribution, including H_2, CO, and CO_2.

At the low-temperature condition (400 ºC), the SR reactions initiate to yield the main products as H_2 and O_2 along with small quantities of CO and CH_4. Finally, at 650 ºC, the SR reaction dominates over all the catalysts, coupled with the formation of CO in small quantities via the RWGS reaction [14]. The bare ALC support did not show any catalytic

activity even at elevated temperatures. Thermal decomposition and ketonization of AcOH led to the formation of the primary products, e.g., H_2 CO, CH_4, CO_2 and acetone, as per Eqs. (Eqs. (1)-(4)) [10].

$$CH_3COOH \rightleftharpoons 2CO + H_2 \quad (1)$$

$$CH_3COOH \rightleftharpoons CO_2 + CH_4 \quad (2)$$

$$CH_3COOH \rightleftharpoons C_2H_4, C_2H_6, \text{coke}\ldots.. \quad (3)$$

- Ketonization

$$2CH_3COOH \rightleftharpoons CH_3COCH_3 + CO_2 + H_2O \quad (4)$$

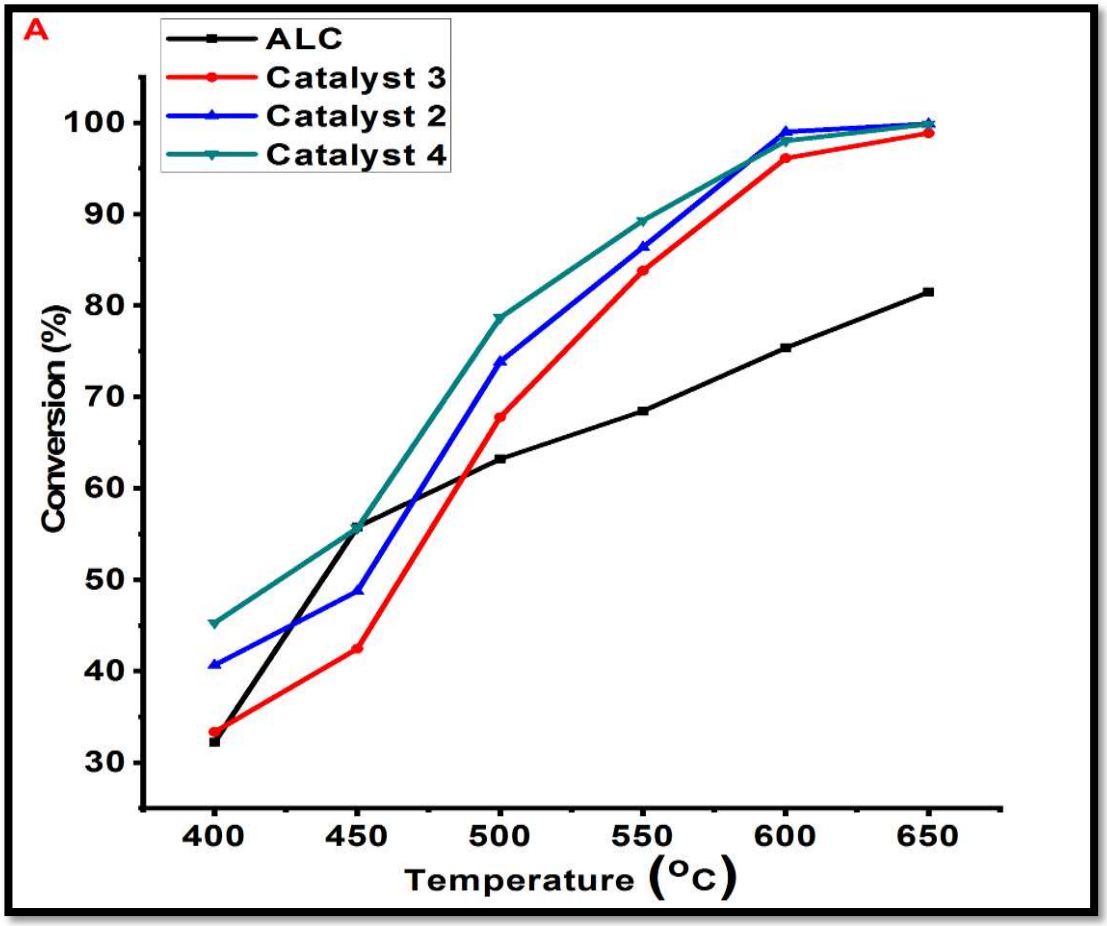

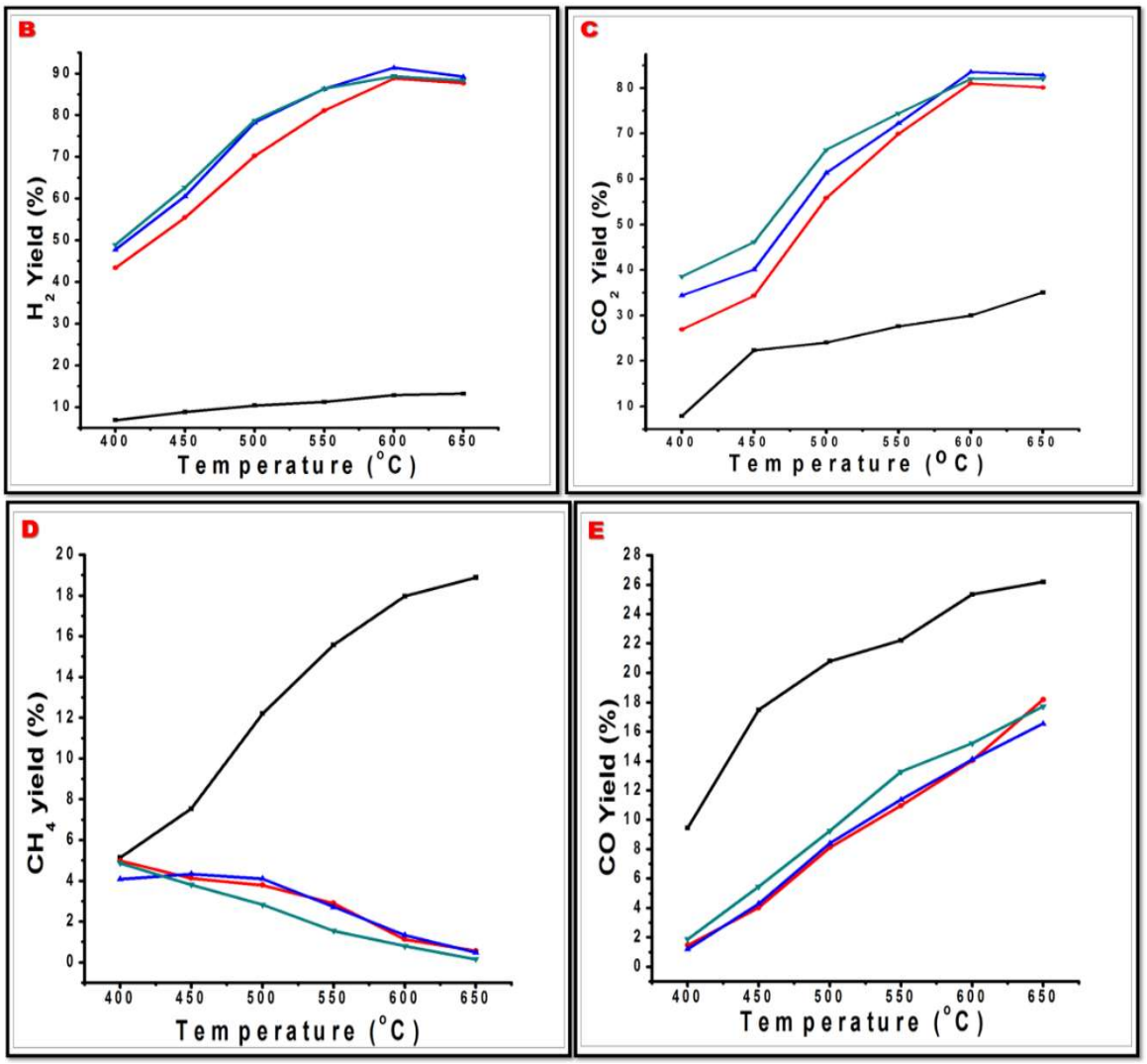

Fig. 5.6. Acetic acid Conversion and the product distribution over reaction temperature and nickel loading; S/C = 6.5; WHSV= 1.2 h^{-1}; P = 1atm

$$CH_3COOH \rightleftharpoons 2CO + H_2 \quad (1)$$

$$CH_3COOH \rightleftharpoons CO_2 + CH_4 \quad (2)$$

$$CH_3COOH \rightleftharpoons C_2H_4, C_2H_6, \text{coke}\ldots.. \quad (3)$$

- Ketonization

$$2CH_3COOH \rightleftharpoons CH_3COCH_3 + CO_2 + H_2O \quad (4)$$

The production of acetone dominates over bare ALC support. CH_4 formation over bare ALC support (**Fig. (5.6 (D))** might come mainly from the decomposition of acetic acid **5.6 (B)** or via other organic intermediate formed since methanation reaction is not prominent because of low hydrogen concentration.

The active Ni phase not only promotes the breakage of C-C and C-H bonds but also promotes the SR of CH_4 at elevated temperatures, as discussed above [15]. The AASR catalytic activities of the catalyst 2, 3 and 4 were not significantly different. Nevertheless, the lowest AASR activity of catalyst 4 may possibly reflect the effect of its low surface area due to large crystallite size and lower pore volume and agglomeration of active metals (Refer Table no. 5.1 and Fig. 5.5). As explained above, a larger Ni crystallite size is primarily responsible for the low surface area of catalyst 4. Therefore, it can be concluded that for achieving higher catalytic activity during the AASR reaction, the Ni loading should be optimized with sufficient active metallic sites and high specific surface area over the catalyst surface.

5.2.2. Effect of Ni loadings on product distributions

The product distribution was greatly affected by the Ni loading during the AASR reaction. Effect of Ni loadings indicate that a sufficient number of active Ni sites are required to achieve high conversion and H_2 yield during the AASR reaction [16]. The CO_2 yield was observed below 18% for all the tested Ni catalysts for lower temperatures, while it was above 80% for higher temperatures. It indicated that the steam reforming reaction dominated over other side reactions (e.g., thermal decomposition, methanation) for all Ni loadings in the observed temperatures range.

The AcOH conversion and product yields are presented in Fig. 5.6 (A-E). The maximum H_2 yield (91.3%) and CO_2 yield (83.54%) were obtained for catalyst 2 at 600 °C. The H_2 yield was seen to rise with an increase in the Ni loading from 0 to 15 wt%, although it declined with a further increase in the Ni loading from 15 to 20 wt%. An increase in the Ni loading also results in a decrease of CH_4 yield while simultaneously increasing the CO yield.

The increment in the loading of Ni present in the catalyst led to an increase in the number of active Ni sites on the catalyst surface, along with the size of Ni particles. The catalytic performance results indicate that the 15 wt% Ni catalyst (catalyst 2) possessed abundant active sites with appropriate Ni particle size, which promoted H_2 production during the AASR reaction. However, greater than 15 wt% Ni loading (catalyst 2) decreased the catalytic activity significantly in terms of H_2 yield. The better performance of 15 wt% Ni catalyst (catalyst 2) than 10 wt% Ni catalyst (catalyst 3) can be attributed to the fact that the former contains large quantities of free Ni sites available for the AASR reaction (as confirmed by the TPR results). Although the 20 wt% Ni catalyst (Catalyst 4) possesses a higher amount of free Ni sites than the 15% Ni catalyst (Catalyst 2), its reduced performance can be attributed to the larger Ni crystallite size and low dispersion. Moreover, a higher Ni content makes the catalyst susceptible to coke deposition, which results in the lowering of catalytic activity with time due to the deactivation of active surface sites. The overall results indicate that Ni loading exerts significantly affects the AcOH conversion and gas product distribution.

5.2.3 Effect of Ni loading over catalytic stability and coke deposition behavior

In order to investigate the resistance to deactivation by coke deposition, a stability test (in terms of AcOH conversion and H_2 yield) of the prepared catalysts was performed for 36 h TOS at 600 °C under atmospheric pressure. The S/C ratio and the weight hourly space velocity (WHSV) values were fixed at 6.5 and 1.05 h^{-1}. As can be seen from Fig. 5.7 ((a)-(b)), both the AcOH conversion and H_2 yield decreased with increasing TOS. The decrease in the catalytic performance with reaction time clearly indicates the deactivation of catalysts due to coke deposition. After 36 h TOS, the AcOH conversion values obtained for 10, 15, and 20 wt% Ni-comp/ALC catalysts were 85.1, 87.3, and 80.9 wt%. Also, the AcOH conversion values for 10 and 15 wt% Ni catalysts (catalyst 2) were observed to be relatively stable after 30 h TOS. Hence,

an increase in the Ni loading from 10 to 15 wt% enhanced the resistance of the catalysts towards deactivation due to coke deposition during the AASR reaction. However, a further increase to 20 wt% Ni loading (catalyst 4) possesses more Ni than all other loadings, presenting less catalytic performance. This fact can be attributed to the large Ni average crystallite size (refer to Table 5.1), leading to high coke formation and catalyst deactivation.

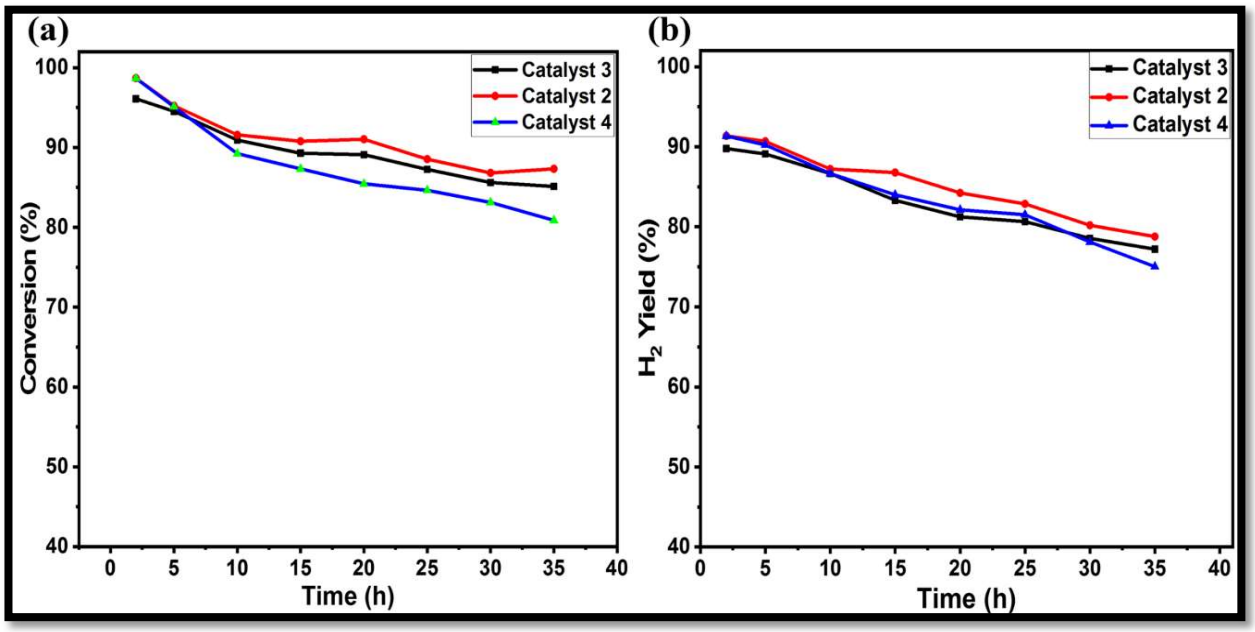

Fig. 5.7. Effect of Ni loading as time on stream **(a)** AcOH conversion and **(b)** H_2 yield

5.3. DT-TGA analysis

The decrease of the weight loss induced by the combustion of coke deposited over the spent catalysts was recorded via the TG analysis shown in Fig. 5.8. (a). The overall weight losses of the catalysts 2, 3 and 4 were computed from TGA graph as 12.77, 10.50, and 17.83 wt%, respectively. Thus, the lowest and highest coke depositions occurred on catalyst 3 and catalyst 4, respectively.

Catalyst 2 displayed higher coke deposition than catalyst 2, possibly due to lower activity towards the AASR reaction. It was found that 20 wt% Ni loading catalyst (catalyst 4) suffered

from serious coke deposition and low activity due to lower dispersion and covering of the active nickel sites with the carbonaceous deposition over prolonged reaction time.

The coke formation process is typically governed by the physicochemical characteristics of the support material, nature of active metallic sites, and the process variables during the reaction. The size and concentration of active metal sites also control the amount and nature of coke deposits formed over the surface of the catalyst [17]. In principle, the amount of coke deposition largely depends on the nickel quantity present over the catalyst surface and on its particle size [17].

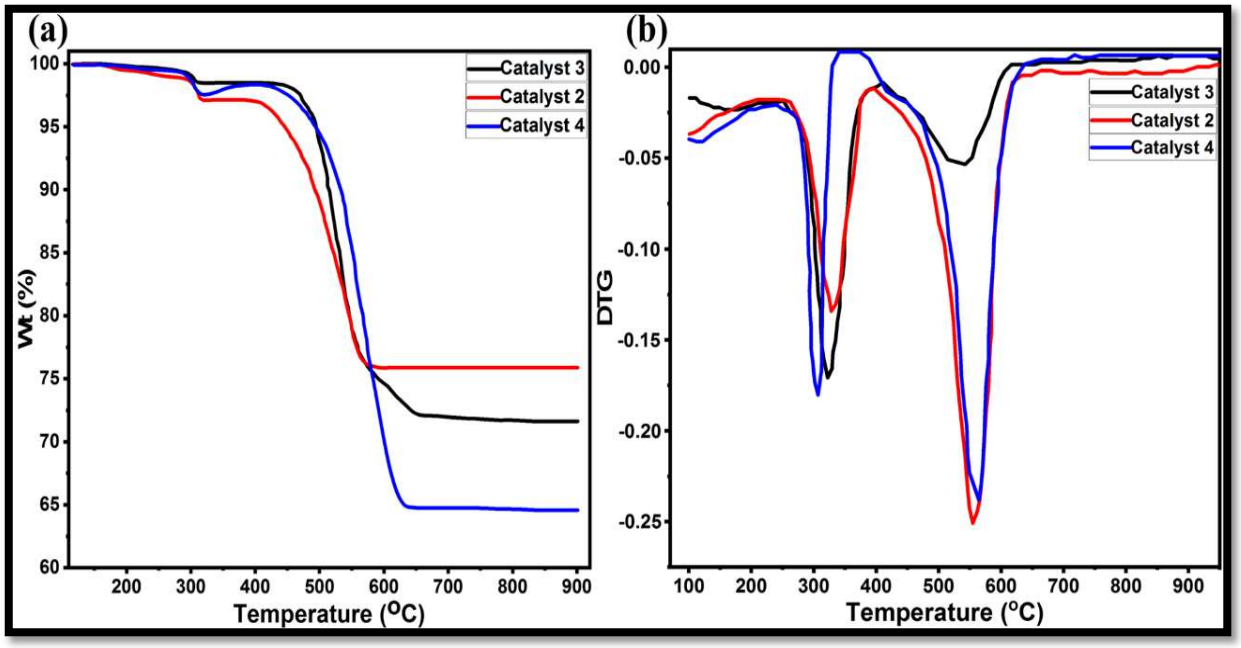

Fig. 5.8. (a) TG and **(b)** DTG analysis of spent catalysts after 36 h TOS

TGA results of spent catalysts showed that 20 wt% Ni loading catalyst (catalyst 4) presented the highest coke deposition formation rate via enhancing the polymerization of carbidic species. However, the higher Ni loading and large particles size of the catalysts lead to lower catalytic performance and higher coke deposition formation. An et al. [18] reported similar observations over Ni/Al_2O_3 with the proposed coke deposition mechanism that could explain the formation of coke deposits over the catalysts surface mainly occurred through AcOH cracking (Eqs. 5-8) and

CO disproportionation reaction (Eq. 8)which consequently reduce their quantity of available active sites.

$CH_3CO_2H \rightarrow (CH_3CO_2)_{ads} + H_{ads}$ (5)

$(CH_3CO_2)_{ads} \rightarrow (CH_3)_{ads} + CO_2$ (6)

$(CH_3)_{ads} \rightarrow C_{ads} + 3H_{ads}$ (7)

$2CO \leftrightarrow C + CO_2$ (8)

The DTG analysis was performed to assess the nature of coke deposition on the catalyst surfaces after 36 h of time-on-stream (TOS) under steady-state conditions. As shown in Fig. 5.8 (b), two characteristic peaks were observed in the DTG profiles. The first peak occurred in the 300-400 °C range, whereas the second peak was observed in the 500-650 °C range. The former corresponds to the amorphous coke deposits (possibly generated via the catalytic cracking of AcOH), while the latter matches the filamentous/graphitic coke deposits (formed through the polymerization of adsorbed amorphous coke or the reactions involving intermediates formed during the AASR process). Similar results have also been reported in the literature [19].

The DTG results indicated that the surface of spent catalyst 3 contained only the amorphous (carbidic species) coke deposits, which are highly reactive to produce the graphitic type coke. Nevertheless, in the case of catalyst 2 and catalyst 4, both types of coke deposits were observed, possibly due to the presence of a large amount of Ni active sites on the catalyst surfaces. Clearly, a higher Ni loading yielded more massive amounts of coke deposits. Furthermore, the results exhibited that increasing Ni loading results in the increased graphitic type of carbon over the catalyst surface due to polymerization of carbidic type carbon at the expense of amorphous carbon. Generally, amorphous carbon grows over support surface, while the graphitic carbon grows over metallic sites [20, 21].

Summary

The effect of Ni loadings over La_2O_3 and CeO_2 promoted γ-Al_2O_3 support prepared via MOF method catalysts were investigated in the 400-650 ºC temperature range for the H_2 production via AASR. The results indicate that the catalytic activity and H_2 yield during the AASR reaction significantly depend on Ni loading. The prepared catalysts achieved almost 100% AcOH conversions at 650 ºC with a high H_2 yield. Small quantities of C1 compounds (CO + CH_4 + CO_2) were also observed to be formed alongside H_2. The characterization results coupled with catalytic activity tests indicate that the 15% Ni catalyst displayed the highest H_2 yield (91.3%) due to abundant free Ni particles with better dispersion. An increase in the Ni loading from 10 to 15 wt% significantly enhanced the AcOH conversion and H_2 yield. A further increase in the Ni loading markedly enlarged the particle sizes of metallic Ni, resulting in lowered AcOH conversion, H_2 yield, and deactivation resistance due to coke deposition. Hence, the catalytic activity and product distribution during the AASR reaction can be closely linked to the amount of Ni present in the catalyst as well as their effective dispersion.

Section: III

Activation, Deactivation and Kinetic studies

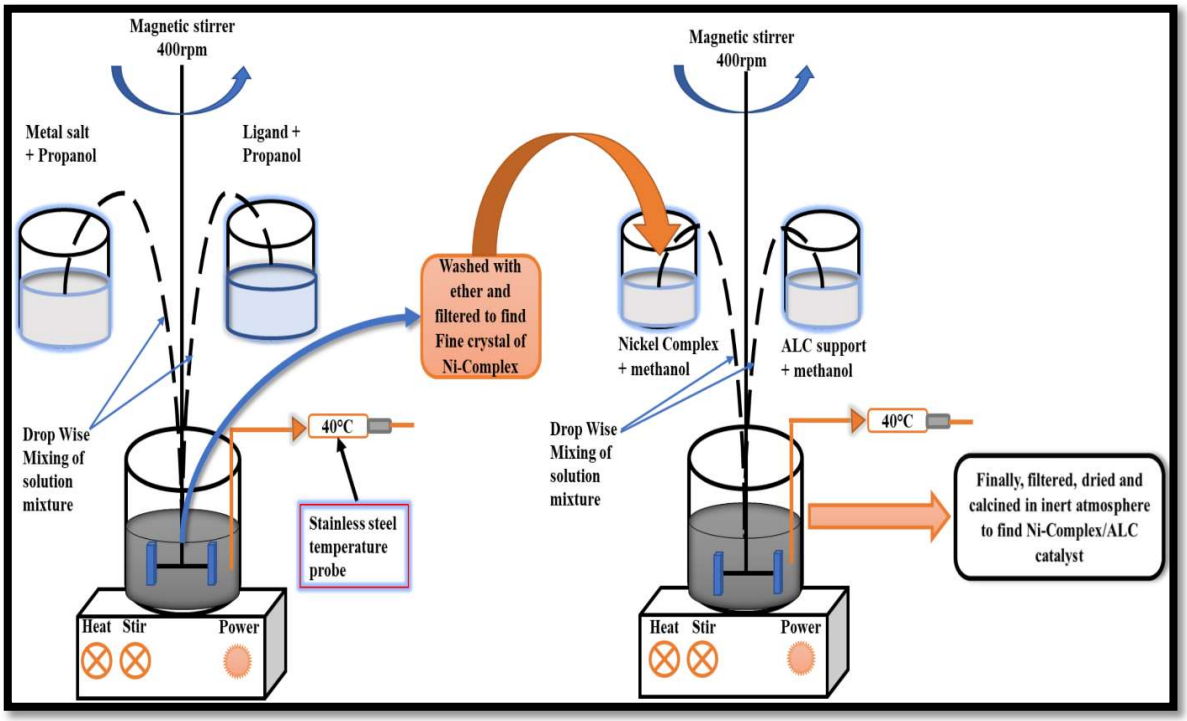

In our earlier section, we have reported that Ni supported on γ-Al_2O_3-La_2O_3-CeO_2 (ALC) catalyst prepared via metal-organic framework (MOF) was more active for acetic acid steam reforming (AASR) [307]. We have also investigated that 15% Ni loading is the best for catalytic activity and H_2 yield. Keeping in mind, here we report a detailed study on the performance of this 15% Ni-complex/ALC catalyst for AASR. Effects of operating conditions such as temperatures (400 - 650 ºC), steam to carbon molar ratio (S/C, 0 to 6.5) and feed flow rate (1.5 to 5.5 mL/h) were evaluated and optimized. Results showed excellent activity for AASR at the molar ratio S/C = 6.5, feed flow rate = 2.5mL/h and 600 ºC with almost total conversion and more than 90% of H_2 yield. The ordered porous structure of embedded nickel-supported catalyst promotes excellent steam reforming activity and water gas shift reaction even at low temperatures, which leads to good stable behavior up to 36 h of TOS. The coke formation was also significantly suppressed by ALC support. Catalysts regenerated by passing oxygen at 500 ºC and followed by reduction in hydrogen also show a good activity. Catalysts were characterized by DT-TGA, XRD, TEM, H_2-TPR and N_2 adsorption-desorption to understand the microstructure and coke deposition behavior.

6.1 Catalysts Characterization

6.1.1 Surface area and pore size analysis

N_2 adsorption-desorption isotherms of the support and fresh catalyst are shown in Fig 6.1. These isotherms are of type IV typically exhibited by mesoporous materials. Textural properties of support and the fresh & the used catalysts as determined by N_2 adsorption isotherms are shown in table 6.1 and table 6.2. The results show that the impregnation of basic oxide promoters (La_2O_3 and CeO_2) on γ-Al_2O_3 leads to loss of surface area as well as the total pore volume of γ-Al_2O_3 support, probably due to the covering of alumina pores

walls by these metal mixed oxides or because of the lower surface area of these metal oxides which have low surface areas.

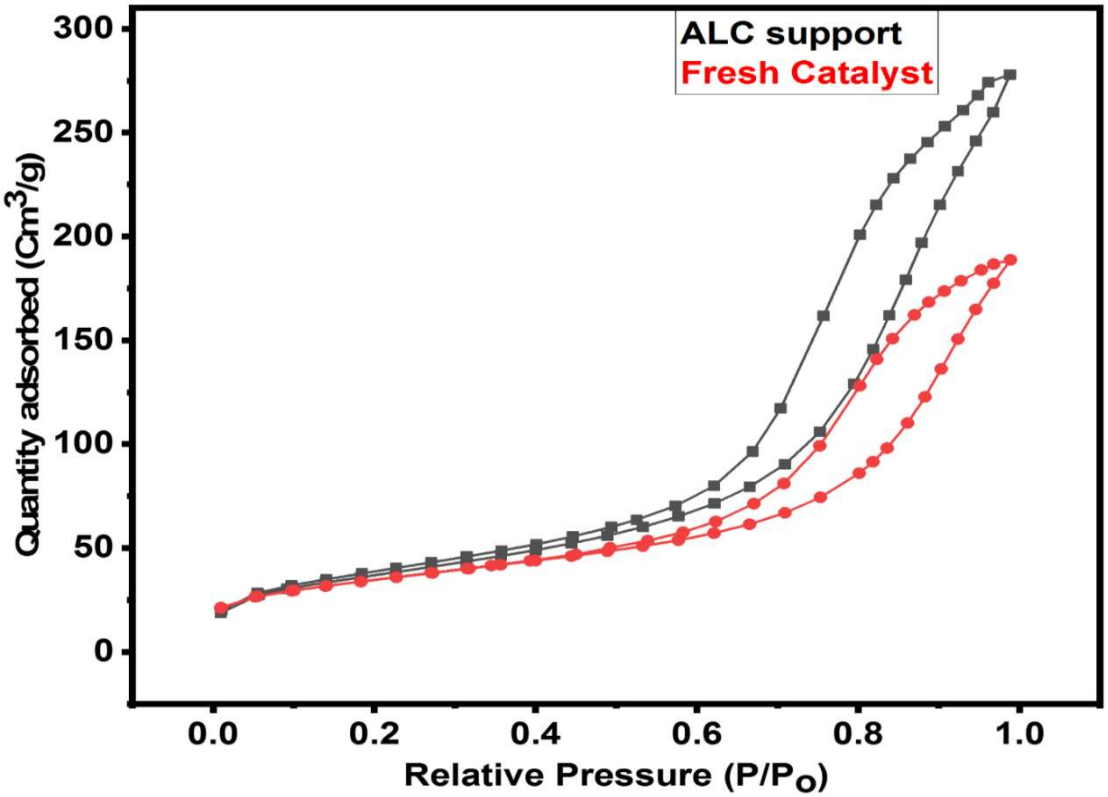

Fig. 6.1 - N_2 adsorption-desorption isotherms of the support and fresh catalyst

Further, incorporation of nickel on ALC support leads to decrease in the surface area as well as the total pore volume.

Table 6.1. Textural properties of synthesized catalysts

Support/Catalyst	Surface area (m^2/g)	Total pore volume (cm^3/g)	Crystallite size of Ni[a] (nm)
Al_2O_3	169	0.61	-
Al_2O_3-La_2O_3-CeO_2 (ALC)	133	0.43	-
Catalyst (Fresh)	120	0.29	37
Catalyst (Deactivated)	84	0.25	-
Catalyst (Regenerated)	110	0.27	40

[a](111) plane

Table 6.2. Pore size distribution of catalysts

Species	Pore size range (Å) and corresponding pore volume (cm^3/g)			
	$0 \le d_p \le 20$	$20 \le d_p \le 40$	$40 \le d_p \le 60$	$60 \le d_p \le 80$
Al_2O_3-La_2O_3-CeO_2 (ALC)	0.38	0.05	-	-
Fresh Catalyst	0.25	0.02	0.01	.01
Deactivated catalyst	0.17	0.04	0.03	0.01
Regenerated Catalyst	0.06	0.13	0.06	0.02

d_p = pore diameter

Pore size distribution (Table 6.2) shows that pores are mostly of size less than 20 Å. It is also observed that the fresh catalyst has a surface area of 120 m^2/g, which is only marginally less than the surface area of ALC support. It is, therefore, concluded that Ni did not lead to any pore mouth blocking of support. On the other hand, nickel was dispersed throughout the porous structure of the support. On deactivation, the surface area has decreased. The deactivated catalyst has 30% lower surface area in comparison to fresh catalyst. On regeneration, catalysts partially regain surface area to a large extent. It is indicative that the deactivation was due to coke deposition. It is further observed from table 6.1 that the total pore volumes do not change significantly. Therefore it is concluded that coke is deposited throughout the pore rather than deposited on the pore mouth and blocking the pores. It is also observed that after regeneration, a fraction of larger pores have appeared (Table 6.2). It is indicative of collapse of pore structures of the support. Large size pores have appeared at the expense of smaller size pores.

6.1.2. XRD analyses of prepared Catalyst

All the XRD patterns of support and the fresh catalyst, deactivated (after 36 h of run at 600 °C, ref. sec. 3.5.4) and regenerated catalyst (the deactivated catalyst regenerated as-

mentioned above in sec. 2.1.3) are presented in **Fig. 6.2.**

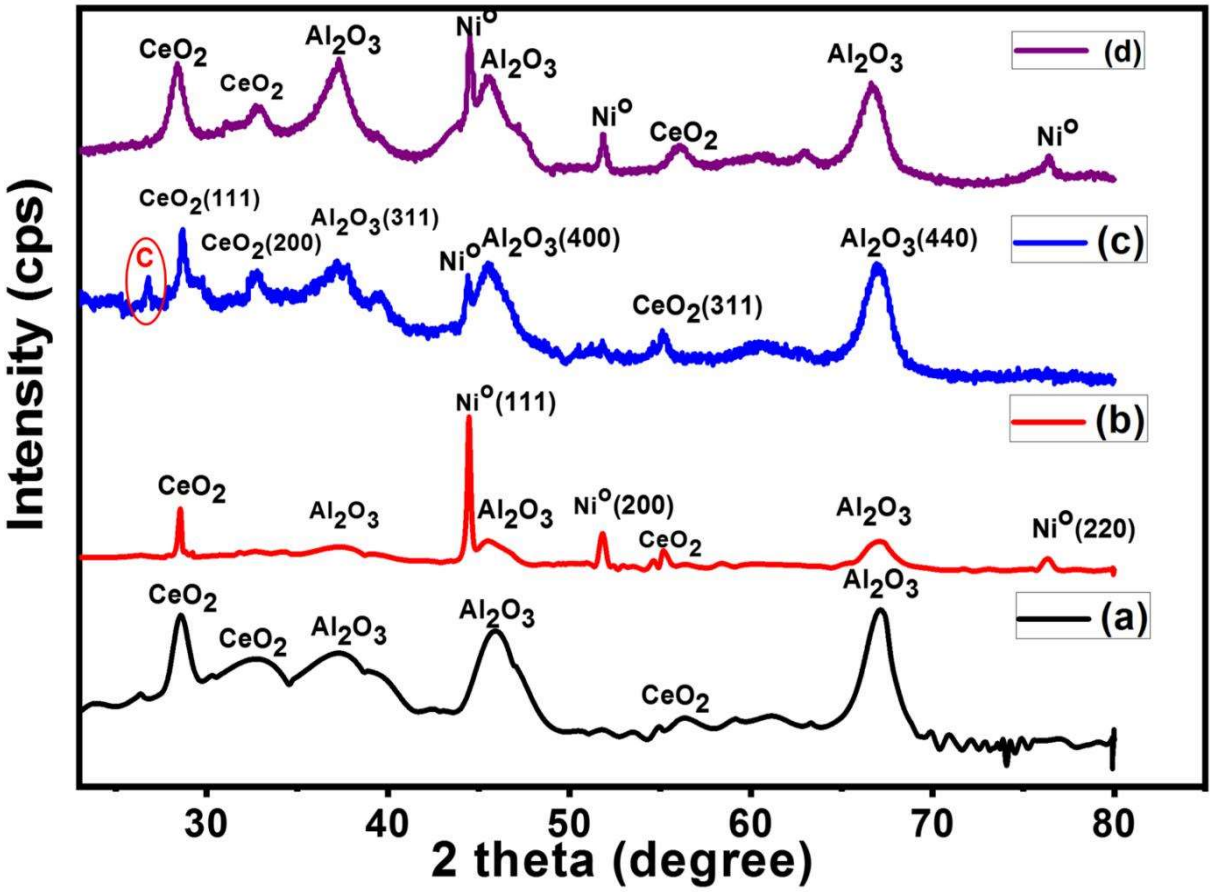

Fig. 6.2 - XRD patterns of **(a)** ALC support, **(b)** Fresh catalyst, **(c)** Deactivated, and **(d)** Regenerated catalyst

Several peaks assigning to supports and metallic Ni were identified with their d-value (calculated using Bragg's law) and matched with the standard values. Peaks correspond to γ-Al_2O_3, CeO_2, and Ni, metal. The MOF-derived Ni particles in the catalyst showed ordered hierarchical aggregates of Ni nanoparticles with 3 dimensions cubic structures. Consequently, it showed good catalytic activity. The support and catalysts showed diffraction peaks at around 2ϑ = 37.2°, 45.8°, and 66.7°, which were assigned to γ-Al_2O_3 (JCPDS 86-1410). The three high-intensity peaks of Ni metal observed at 44.5°; at 51.8° and 76.5° correspond to (111), (200) and (220) planes. No characteristic peak of NiO at 2θ = 37.3° and 43.3° (JCPDS 78-0643) present or corresponding to $NiAl_2O_4$ could be identified. Catalysts also showed the characteristic peaks of cubic fluorite crystal structure

of CeO_2 at 2θ =28.30º (111), 33.13º (200) and 56.33º (311) in catalysts and the support ALC respectively, which shows the segregation of the CeO_2 over the γ-Al_2O_3 [279]. Cubic fluorite structures also help to diffuse more oxygen and formation of oxygen vacancy[99]. No peak of La_2O_3 was observed in either of the catalysts or in ALC support, probably due to the well dispersion and low amount of La_2O_3 in the catalysts [45]. The XRD diffraction patterns of prepared catalysts indicated that nickel observed was mainly metallic phase only on the synthesized support. It is also noteworthy that all the peaks corresponding to the nickel particles are in the highly ordered regular cubic structured over the surface of ALC support. The average crystallite size of the catalysts (fresh, deactivated and regenerated) was calculated by Scherrer equation for the (200) peak, and results are shown in **Table 6.1.** It is observed that the crystallite size of Ni in fresh catalyst had 37nm, while in the case of deactivated catalyst, Ni° peak for the same plane (200) disappeared due to covering of coke formation. The Crystallite size in the regenerated catalyst was 40 nm, nearly equal to that of the fresh catalyst. Which represents coke has been gasified from the catalyst surface after the regeneration process. The XRD patterns of the deactivated catalyst after 36 h reaction showed a peak 2θ = 26.5º, attributed to graphitic carbon deposition on catalyst during reforming reaction. Above results lead to the conclusion that the deactivation of catalyst was due to deposition of coke on the surface. The DTA results, as discussed later, have shown that the deposited coke was of two types; i.e., amorphous and graphitic. Further, any significant sintering of nickel particles was not observed. Hence, it is not considered to be a cause of the deactivation of the catalyst.

6.1.3. TPR Analysis

TPR profiles of oxidized nickel-supported catalyst and unsupported nickel oxide are shown in **Fig. 6.3.** Reduction of pure NiO (unsupported), referred to as free nickel oxide, NiO to Ni is observed at 329 ºC [308].

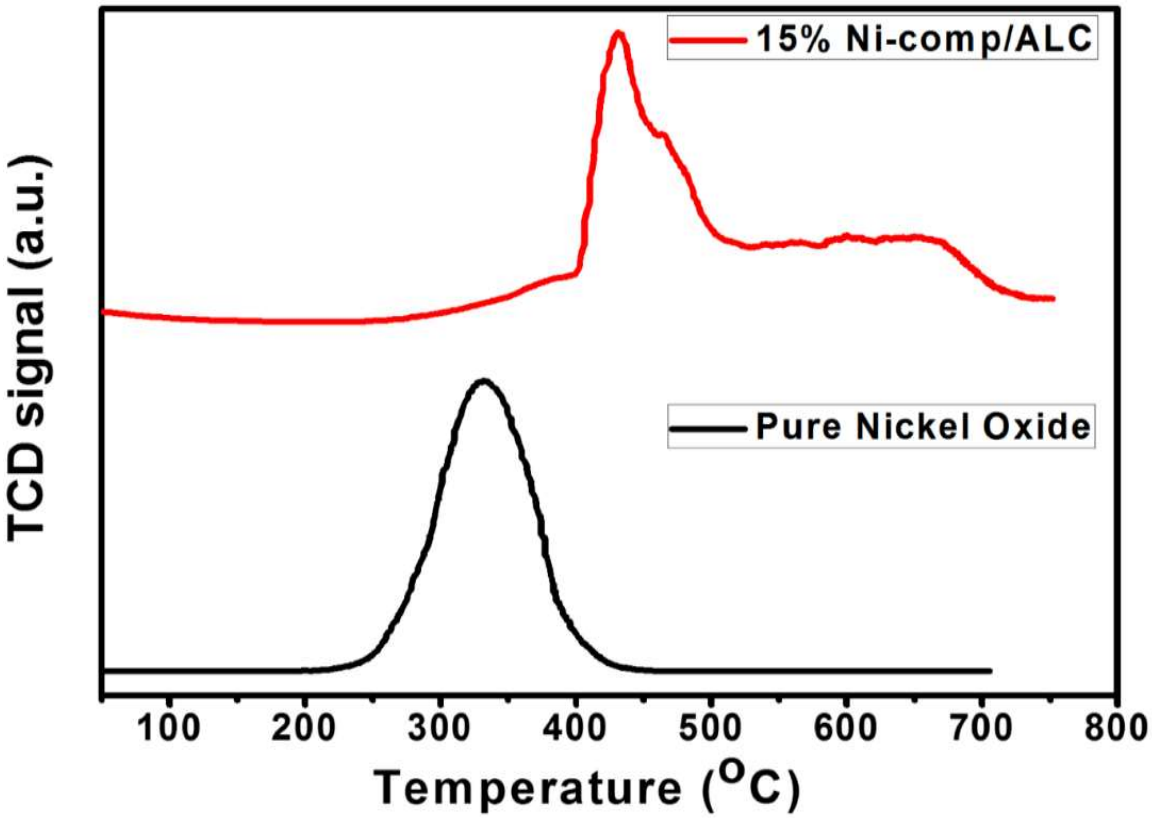

Fig. 6.3 - TPR profiles of 15%Ni-Comp/ALC catalyst and pure NiO

However, a shift in the reduction peak(s) is observed in catalyst compared to the reduction temperature of unsupported NiO. The catalyst showed a reduction peak at a higher temperature of 406ºC with a hump at 437 ºC. In general, the metal support interaction hinders the sintering of metal particles. In the present study, the crystallite size of Ni was almost stable after 36 h of run. This observation is attributed to the metal-support interaction observed in the catalyst. The use of a metal-organic framework precursor might have resulted in formation of metal-support interaction in the catalyst.

6.1.4. SEM analysis of Fresh and Spent catalyst

Comparison of SEM observation of fresh and spent 15%Ni-Comp/ALC catalysts are shown in the above **Fig. 6.4 (A-B)** finds that graphitic type carbon is formed overspent catalysts in comparison to the fresh catalyst, but the catalyst still contained rich porous structure and unblocked sites of nickel.

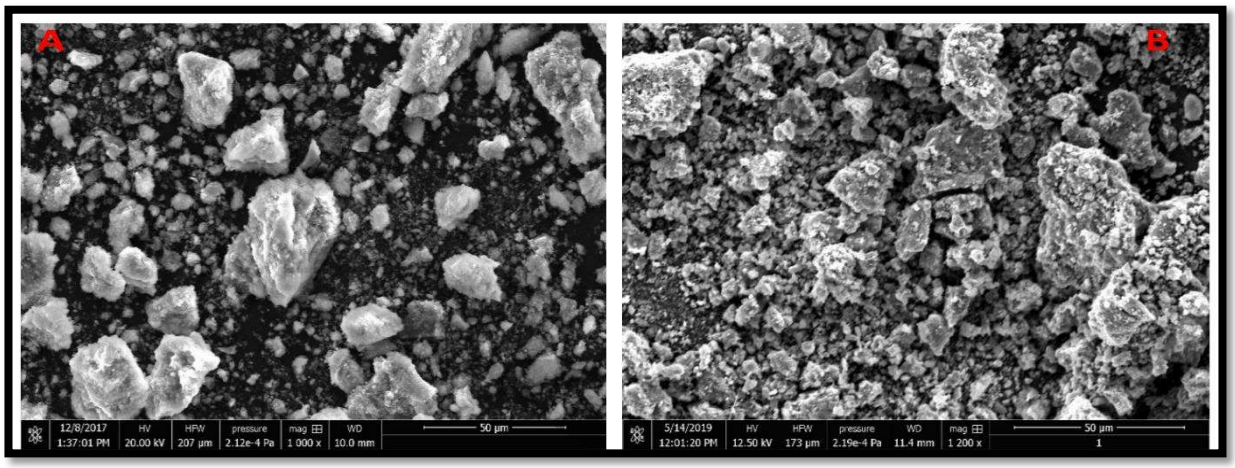

Fig. 6.4 (A) 15 % Ni-Comp/ALC (Fresh) **(B)** 15% Ni-Comp/ALC (Spent) after 36h

6.1.5. DT-TGA analysis of spent catalyst

In order to determine and characterize the deposited coke over spent catalyst during steam reforming reactions, DT-TGA analysis of used catalysts was carried out. TGA of the used catalysts was carried out in the presence of oxygen from room temperature to 1000 °C with a heating rate of 10 °C /min shown in **Fig. 6.5.**

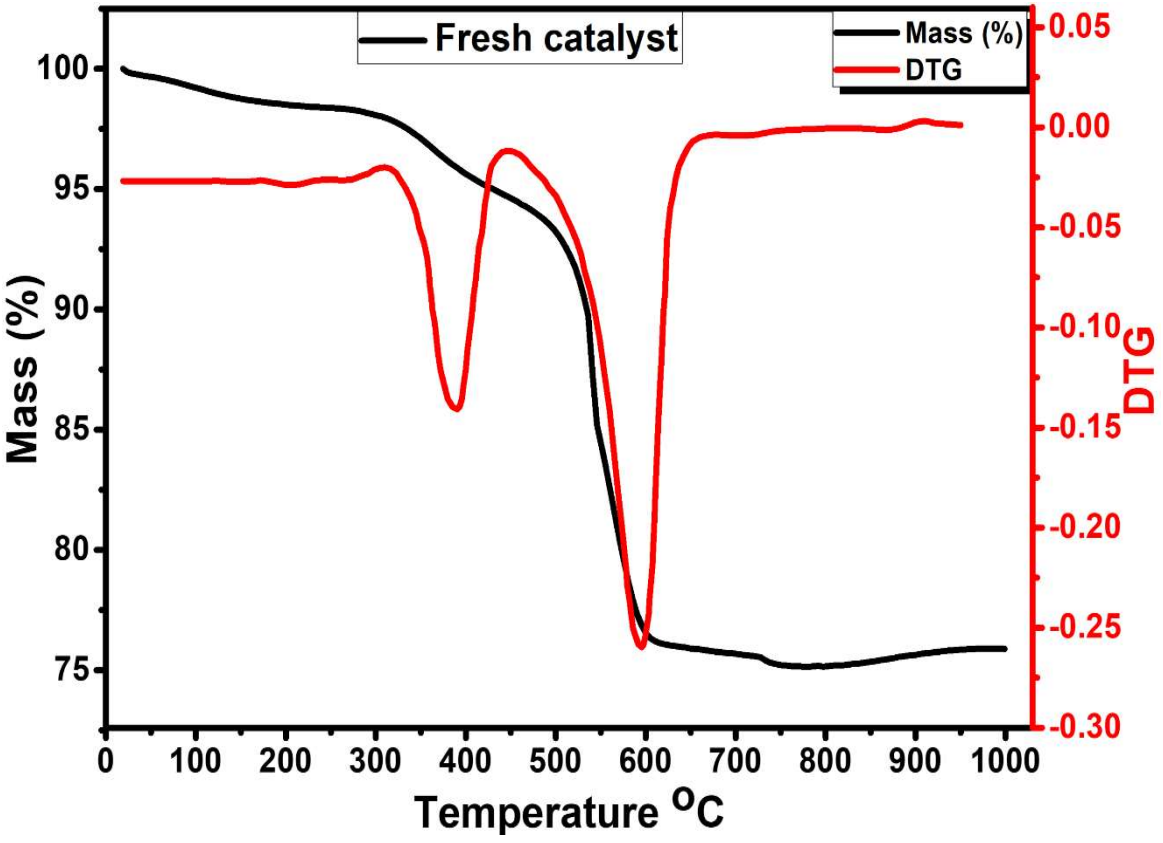

Fig. 6.5 – TG-DTA analysis of fresh catalyst after 36 h TOS deactivation

The weight loss of the spent catalyst (catalyst after 36 h TOS) was observed around 24.1 %. Two types of coke species were found on the surface of the catalyst. The first peak observed at lower temperatures between 350 - 400 °C has been attributed to coke combustion/oxidation of amorphous carbon. The second peak that appeared between 500-550ºC is attributed to oxidation of graphite or filamentous carbon associated with nickel particles [33, 218]. It has been reported that the amorphous type of coke generally unstable and easily oxidizable. It has been observed that for regenerated catalyst after 36 h TOS reaction, the coke formed over the catalyst surface via both types of carbon (amorphous and filamentous/graphitic) contributed in higher proportion. To mention that, the filamentous/graphitic coke formed over metallic sites showed comparatively less effect than amorphous coke on catalytic performance [33].

6.2 Activation, deactivation and regeneration studies

The stability of catalysts was performed at fixed operating conditions (Temp - 600 °C, Feed flow rate -2.5mL/h and S/C -6 mol/mol). Regeneration of deactivated catalyst at 600 °C was performed in-situ in a fixed bed reactor by passing oxygen with a 60 mL/min flow rate at 500 ºC for 3 h. The objective was to burn off deposited coke on the surface of the catalyst. Subsequently, it was cooled down to room temperature, and H_2 at 600 ºC was blown over the catalyst for 3 h. It ensured that any oxidized nickel was reduced in the regenerated catalyst.

6.2.1 Effect of temperatures

Conversion of acetic acid and yield of products as a function of temperature are shown in Fig 6.6. Experiments were performed in the temperature range of 400 and 650 ºC with 2.5mL/ h (acetic acid/water mixture as feed) feed flow rate, S/C (steam to carbon in the feed) ratio of 6.5, and 0.5g of catalyst. All the product samples during experiments were collected after achieving steady state. It was approximately 4 h after starting the run. All

the experiments related to conversion, yield and stability tests of catalyst were performed at least twice for the same operating conditions (e.g., temperature, feed flow rate and S/C ratio), and all the data were collected when the temperature became constant at the desired value for at least 30 min with a deviation of less than 5 °C.

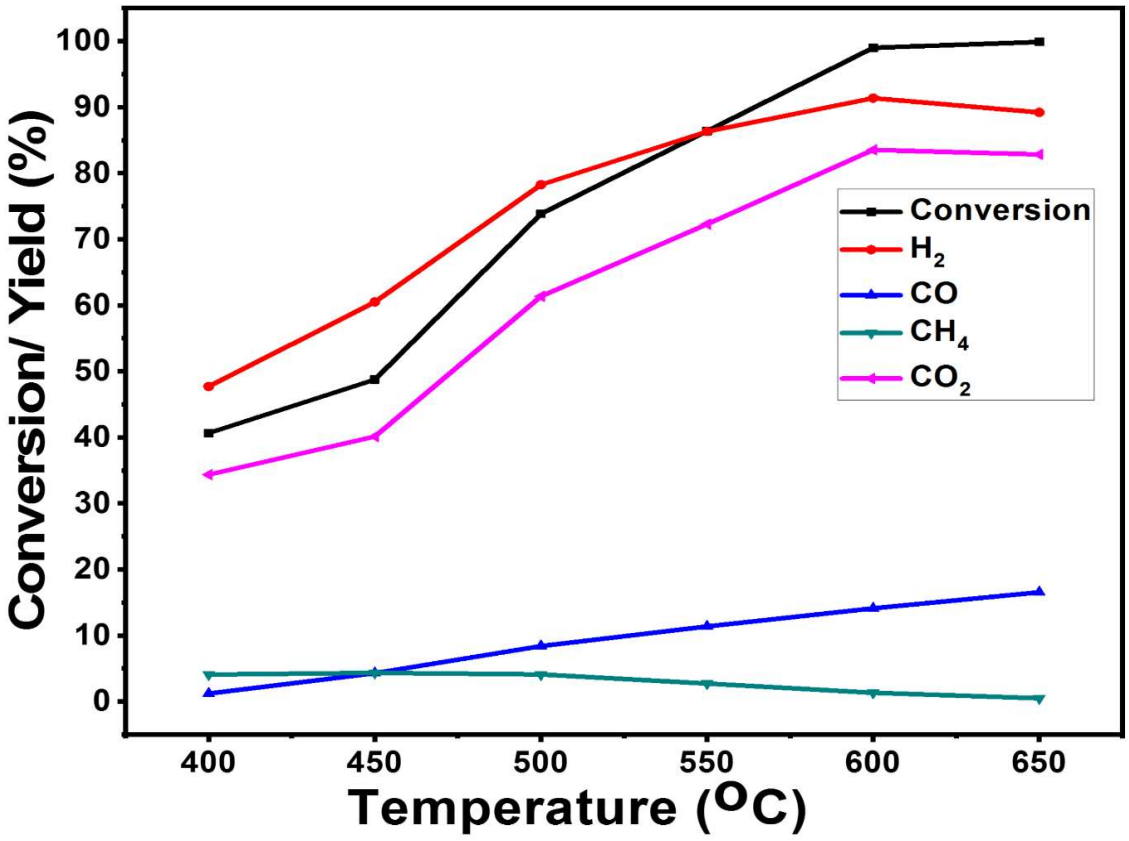

Fig. 6.6 Conversion and yields of products over 15%Ni-Comp/ALC: S/C = 6.5, Feed flow rate = 2.5mL/h, P = 1 atm

The experimental data produced were approximately the same with a marginal difference. The average values have been reported in the data. It could be seen from Fig. 8 that catalyst showed activity for the reforming reactions even at an initial lower temperature of 400 ºC, where conversion of acetic acid reached about 40.44%. There were four major products; H_2, CO, CH_4, and CO_2. The conversion of acetic acid increased upon increasing reaction temperature up to 600 ºC. Our results matched the results obtained by previous research [181]. The production of methane decreased as temperature increased. During AASR, CH_4 is produced via thermal decomposition of acetic acid and the methanation of CO and

CO_2[16]. However, according to a thermodynamic study, CH_4 formation occurred mainly via thermal decomposition at higher temperatures. The formation of CH_4 at high temperatures was almost negligible because at high-temperature CH_4, the steam reforming reaction become favorable [309]. The production of CO increased monotonously with the increase in reaction temperatures. At high reaction temperature CO was produced possibly via the reverse water gas reaction (RWGS), whereas at lower temperatures, CO production might come from the thermal decomposition of acetic acid as catalyst showed poor activity towards RWGS [305]. H_2 yield increased with increasing temperature, in the line of the thermodynamics prediction[181]. In previous research, similar trends were observed when Ni and Co-based catalyst were studied during AASR. The C-C bond cleavage conversion and gaseous yields (H_2, CO, CO_2) were increased with increasing temperatures [310]. From the results, it was observed that H_2 yield increased until 600 ºC and then decreased. The yield of CO_2 also increased up to 600 ºC and decreased slightly after 600 ºC. The decrease in H_2 and CO_2 yield at high temperatures have been attributed to the RWGS reaction. Which was favored at high reaction temperatures consequently dropped the concentration of H_2 and CO_2. In the temperatures range of 400–650 °C, almost complete conversion of acetic acid was obtained, and H_2 yield was 91.36 % was achieved at 600 ºC.

6.2.2 Effect of feed flow rate

The effect of acetic acid mixture flow rate was studied at a constant carrier gas flow rate and steam to carbon molar ratio (S/C = 6.5) at 600 ºC shown in **Fig. 6.7.** The mixture flow rate was varied between 1.5 to 5.5mL/h. Although the feed flow rate of AcOH mixture did not have much effect on the conversion of acetic acid, however, H_2 and CO_2 yield declined significantly at higher flow rate due to the reduction in C-C bond cleavage and due to decrease in contact time between reactants and catalyst that prevents steam reforming process and dominate decomposition reaction.

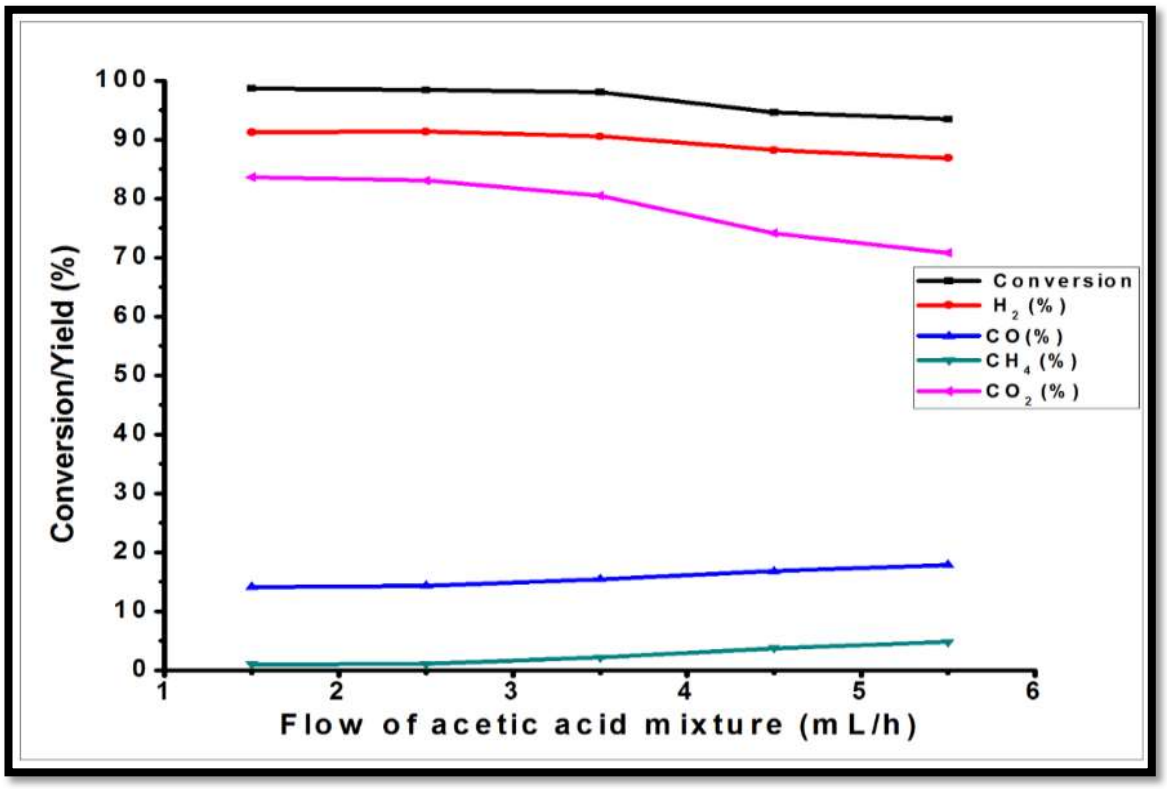

Fig. 6.7 Effect of the feed flow rate of AcOH mixture on conversion and yield of products over 15 wt%Ni-Comp/ALC; Temp 600 ºC, S/C ratio - 6.5: 1, P=1atm

Takanabe et al. explained reaction pathways of AASR and reported that H_2, CO, CH_4 and CO_2 were the main products formed via decomposition of CH_x species. C-C bond cleavage played a significant role in acetic acid steam reforming [132]. With the increase in the feed flow rate, the yield of other by-products such as CO and CH_4 increased remarkably. At 600 °C, CO was produced as a secondary by-product, probably due to RWGS reaction. It was observed from the results that at high feed flow rates, low conversions and high CO and CH_4 production probably, the interaction between reactants and catalysts decreased, which suppress the steam reforming reaction[214]. From **Fig. 6.7,** it is also observed that increasing the feed flow rate, H_2 and CO_2 yield percentage decreased, whereas CH_4% increased. It is attributed to the fact that at low feed flow rates, the interaction of the reactants with the catalysts was excellent, improving steam reforming reaction dominated over thermal decomposition, leading to a higher yield of H_2 and CO_2. Whereas at higher

flow rates, owing to lesser contact time with catalyst, thermal decomposition dominated over steam reforming.

6.2.3 Effect of steam to carbon molar ratio (S/C)

Steam/carbon molar ratio (S/C) is an important parameter in the steam reforming process. A high S/C ratio prevents coke formation on the catalyst surface and results in a better yield towards H_2. Therefore, the effect of S/C was examined at 600 ºC (reaction temperature at which yield of hydrogen was the highest) and constant feed flow rate of the mixture. Fig. 6.8 showed the results where acetic acid conversion and product distribution were plotted as a function of the S/C molar ratio. It is observed from the figure that both conversion and yield of acetic acid increased for H_2 and CO_2 monotonously with an increase in S/C ratio from 0 to 6.5 and further increase these levels off.

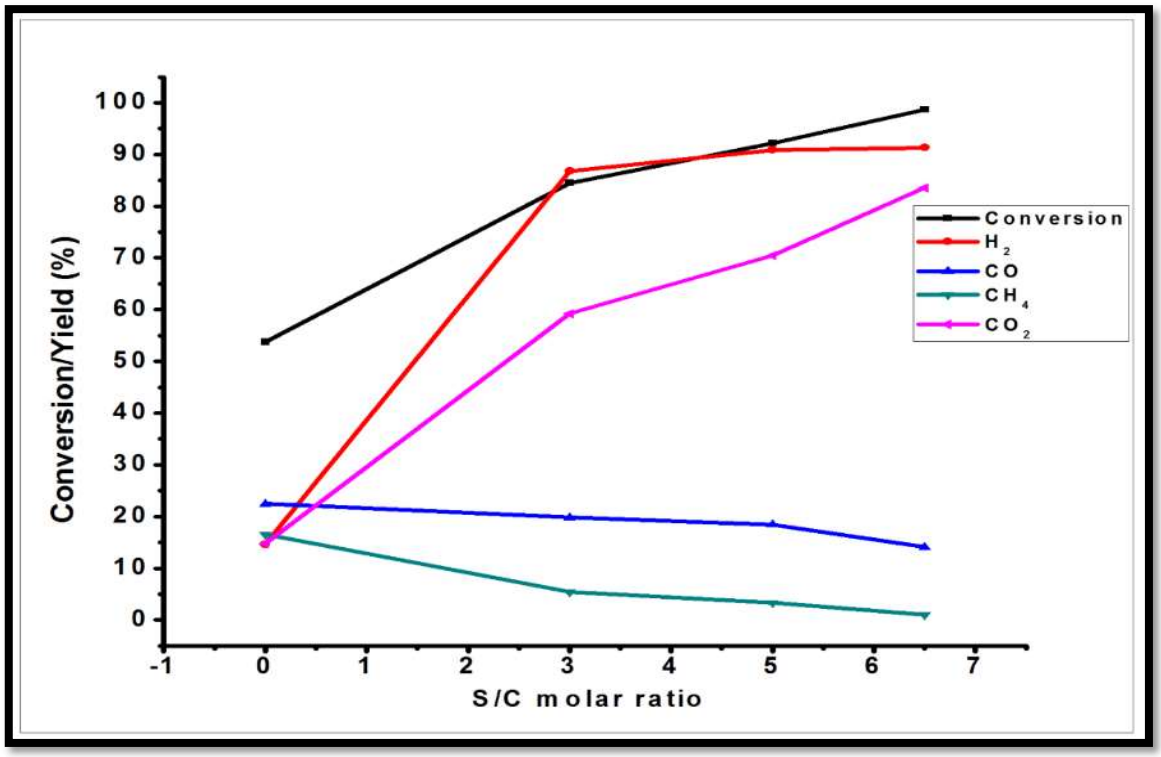

Fig. 6.8 Effects of S/C ratio on the conversion of AcOH and product distribution over 15%Ni-Comp/ALC at 600 ºC, Feed flow rate– 2.5 mL/h, and P-1atm

On the contrary, the formation of by-products (CO, CH_4) decreased in a high S/C ratio. At low S/C ratio, decomposition reactions of acetic acid are favored according to Eqs (1) and

(2), leading to a large amount of CO and CH_4. During AASR, the adsorption of steam on the catalyst surface plays a crucial role in suppressing the formation of by-products (CO, CH_4, C_2H_4, CH_3COCH_3) via the promotion of water gas shift (WGS) reaction but enhances the removal of carbonaceous desorption also over the catalyst surface. A high S/C ratio promotes steam adsorption over the catalyst surface because of increased partial pressure [311].

It is observed from the results that additional steam can favor steam reforming reactions and suppress the generation of by-products. Similar results have been reported by Marquevich et al. [85] that a lower S/C ratio would favor the lower rate of steam reforming reaction and consequently generation of a large amount of by-products due to the low partial pressure of steam. Phongprueksathat et al. also reported that $Ni/Ce_{0.75}Zr_{0.25}O_2$ (CZO) supported catalyst promotes C-C bond cleavage activity and increased H_2 yield at a higher S/C ratio[310]. Moreover, it could be seen from the results that at S/C = 0, the yield of H_2 is very low due to the absence of acetic acid steam reforming reaction, and the governing reactions are decomposition and ketonization. While, in the presence of steam, reforming reactions are dominated, and these reactions depressed significantly. As the S/C ratio increases from 0 to 3, the steam reforming reaction dominated. As a result, the conversion and yield of H_2 increased remarkably.

However, due to the significant amount of CO generation, the yield of H_2 was still relatively low. The reason for this is that it was more difficult to remove CO from shift reaction in low steam ratios. The later runs made in the high S/C ratio demonstrated that CO yield decreased with increasing the S/C ratios. It is observed that at higher S/C ratios, the WGS reaction response was promoted, and the RWGS reaction was interrupted comparatively. As shown in **Fig. 6.8,** S/C = 6.5 and temp 600 ºC were required for the maximum H_2 yield during AcOH steam reforming for hydrogen production.

6.2.4 Catalyst stability and regeneration studies

Several researchers have reported that catalyst deactivation is mainly because of the formation of severe coke deposition on catalytically active sites [33, 85, 312]. Keeping in mind that the catalyst exhibited the best conversion and selectivity of H_2 at T = 600 ºC, S/C = 6.5 and mixture flow rate 2.5 mL/h. The stability of the catalyst was performed at these conditions. The stability test was performed for 36 h, and the result showed the dependence of the acetic acid conversion and H_2 yield on the reaction time on stream (TOS). As displayed in **Fig. 6.9,** initially, with the reaction time of 20 h, both conversions of acetic acid and the yield of H_2 over the 15 wt% Ni-Comp/ALC reduced. After 20 h TOS, AcOH conversion and the yield of H_2 did not change much after more than 36 h of reaction. The fresh catalyst conversion declined from 98.69 to 93.73% in 36 h, and the yield of H_2 decreased from 91.36 to 87.26% after 36 h of reaction.

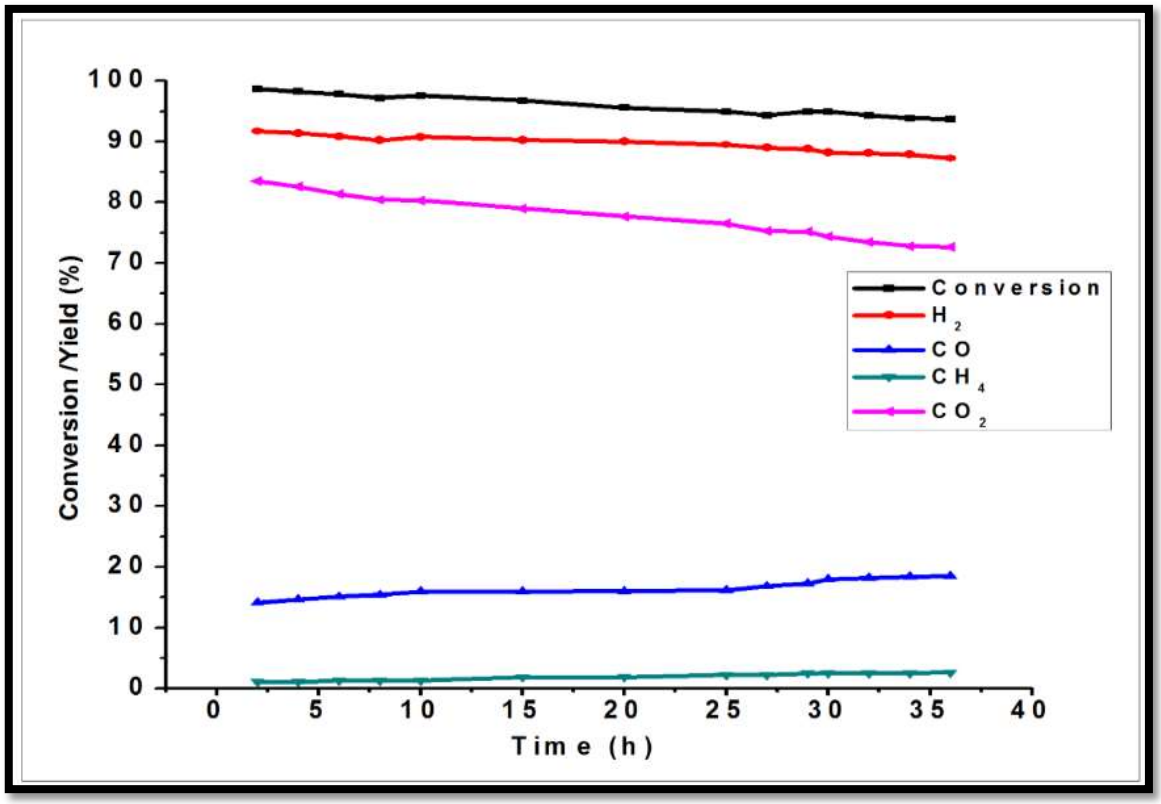

Fig. 6.9 AcOH conversion and yield of gaseous product versus reaction time over 15%Ni-Comp/ALC catalyst. Reaction condition: temperature-600 ºC; N_2; Feed flow rate-2.5 mL/h; and S/C- 6.5

The deactivation of the catalyst was mainly due to the coke deposition over the active sites. Coke deposition occurs mainly due to polymerization or thermal decomposition of acetic acid or reaction intermediates at high temperatures [214]. The spent 15 wt% Ni-Comp/ALC catalyst after 36 h was characterized by CHNS analysis; the total carbon % deposited was 23.46 wt%. As discussed earlier, the types of coke deposited on the surface of catalyst were further characterized with DT-TGA in the air. Lu et al. [313] have studied the coking and regeneration of Ni/γ-Al_2O_3 catalyst and the effect of coke nature. They reported that the catalyst was deactivated due to toluene cracking at 700 °C within 0.5 h. The deactivated catalyst was repeatedly regenerated by calcining in the air at 600 °C for 3 h. Results showed excellent conversion even after the third regeneration, and a filamentous type of coke was formed over the catalyst surface. Wang et al. [314] also reported that supported Ni/Al/Mo spent catalysts after hydrogenation reaction of hydrocarbon were regenerated by passing oxygen at 550 ºC for 3 h and suggested that at lower temperature coke could not be oxidized completely, whereas, at high-temperature, sintering of catalyst might occur. Therefore, regeneration of deactivated catalyst was performed in-situ in the reactor by passing oxygen with a 60 mL/min flow rate at 500 ºC for 3 h and subsequently cooled to room temperature and reduced in the presence of H_2 at 600 ºC for 3 h. The conversion and product distribution of regenerated catalyst is also displayed in **Fig. 6.10.** It was observed that catalyst activity was approximately regained after regeneration. The slightly lower performance of regenerated catalyst slightly lowered compared to fresh catalyst may be due to the increase of Ni crystallite size (from 37 to 40 nm) as well as due to structural change in the support as observed in pore size analysis (Refer Table 6.1 & 6.2). The SEM analysis also showed that only marginial coke deposition occurred over the catalyst surface because of that showed high stability of both fresh and regenerated catalyst.

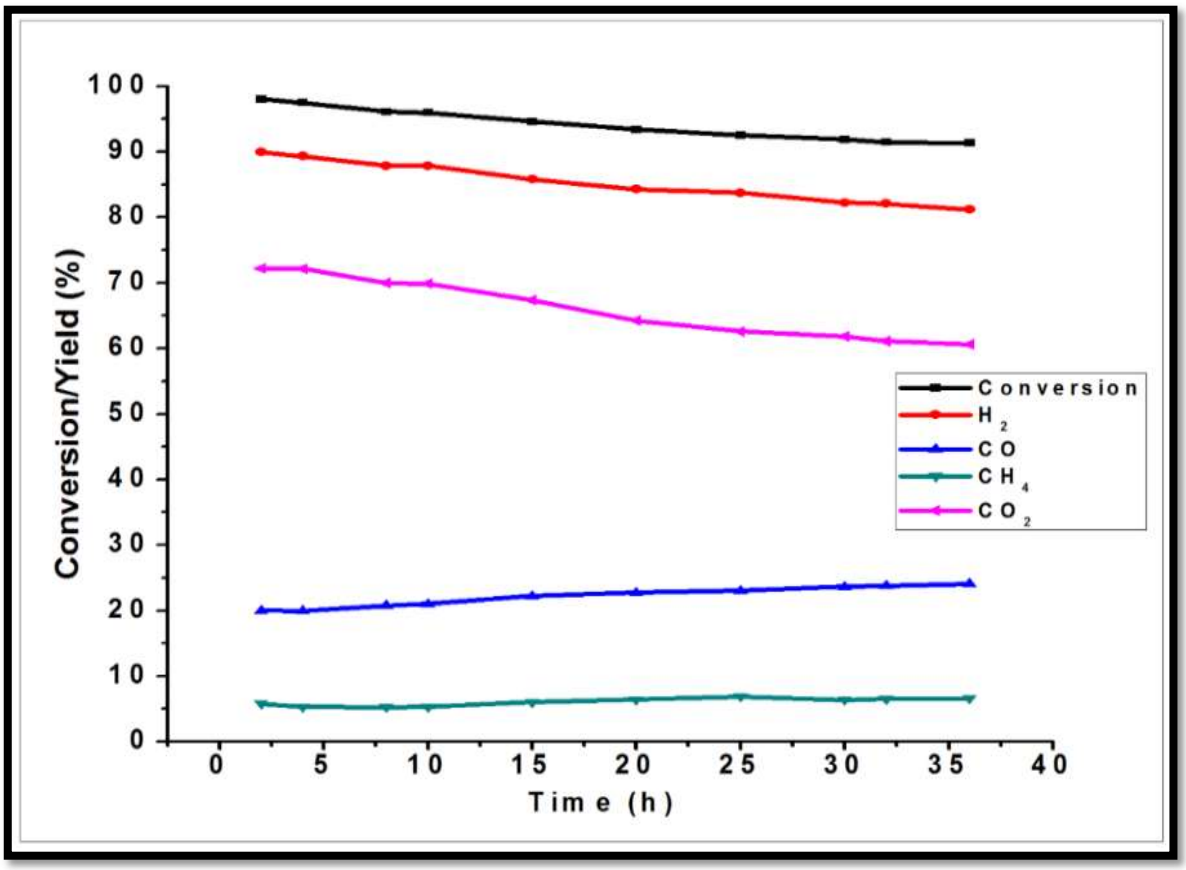

Fig. 6.10 AcOH conversion and yield of gaseous products versus reaction time over regenerated 15% Ni-Comp/ALC catalyst. Reaction condition: temperature-600 ºC; N_2 flow rate- 30mL/min; feed flow rate - 2.5 mL/h; and S/C- 6.5 mol/mol

Summary

A new porous ordered Ni-Complex/ALC catalyst was synthesized via the MOF process was investigated. At constant operating conditions (S/C = 6.5, feed flow rate = 2.5mL/h), the increase in the temperature range from 400 - 650 ºC conversion increases while in the case of H_2 yield it increases up to 600 ºC and then slightly decreases after 600 ºC due to RWGS reaction dominating at high temperature. The results showed that during the AASR, H_2, CO, CH_4, and CO_2 were the main product gases, whereas a maximum hydrogen yield of 91.3% was obtained at temperature 600 ºC. The temperatures and S/C ratio were the key parameters, while the feed flow rate of the AcOH/H_2O mixture showed only a marginal effect during AASR. The catalyst was deactivated by coke deposition. Amorphous and graphitic types of coke were found to get deposited on the surface of the deactivated

catalyst. Deactivated catalyst had lower surface area and pores of larger diameter compared to those of fresh catalyst. The deactivation studies of Ni-Complex/ALC catalyst showed excellent stability up to 36 h TOS. Catalyst regeneration of spent catalyst was achieved by flowing oxygen over the catalyst at 500 ºC, followed by reduction by H_2 gas. Regenerated catalyst regained the surface area, pore-volume, and nearly the same activity as a fresh catalyst. The sintering of Ni particles was not significant. It has been attributed to the existence of nickel-support interaction.